Supporting Information

Quenching-induced lattice modifications endowing Li-rich layered cathodes with ultralow voltage decay and long life

Lingcai Zeng,‡[ab] Haoyan Liang,‡[a] Yaqian Wang,[a] Xiaolong Ying,[a] Bao Qiu,*[ac] Jiajie Pan,[b] Yibin Zhang,[a] Wen Wen,[d] Xuechun Wang,[e] Qingwen Gu,[a] Junhao Li,[b] Kaixiang Shi,[b] Yanbin Shen,[e] Quanbing Liu*[b] and Zhaoping Liu,*[ac]

[a] Ningbo Institute of Materials Technology and Engineering (NIMTE), Chinese Academy of Sciences (CAS), Ningbo 315201, PR China

[b] Guangzhou Key Laboratory of Clean Transportation Energy Chemistry, Guangdong Provincial Key Laboratory of Plant Resources Biorefinery, School of Chemical Engineering and Light Industry, Guangdong University of Technology, Guangzhou 510006, China

[c] Center of Materials Science and Optoelectronics Engineering, University of Chinese Academy of Sciences, Beijing 100049, China

[d] Shanghai Synchrotron Radiation Facility, Chinese Academy of Sciences, Zhangjiang High-Tech. Park, Pudong New Area, Shanghai, China

[e] i-Lab, Suzhou Institute of Nano-Tech and Nano-Bionics (SINANO), Chinese Academy of Sciences, Suzhou 215123, China

† Electronic supplementary information (ESI) available.

‡ These authors contributed equally to this work.

* E-mails: qiubao@nimte.ac.cn, liuqb@gdut.edu.cn and liuzp@nimte.ac.cn

Experimental section

Materials synthesis

Conventional co-precipitation method was taken to prepare precursors of Li-rich layered cathode materials $Li_{1.187}Ni_{0.136}Co_{0.136}Mn_{0.533}O_2$ (denoted as LLO). The detailed procedure was described in our previous report.[1] First, a 2.0 mol L^{-1} solution of nickel, cobalt, and manganese sulfate was pumped stoichiometrically (Ni: Co: Mn=1:1:4) into a 50 L continuously stirred tank reactor (CSTR) for the co-precipitation reaction. 2 mol L^{-1} Na_2CO_3 and 0.2 mol L^{-1} ammonia mixed aqueous solution were used as precipitant and complexing agent. The reaction pH was controlled at 7.0 ~ 8.0, the reaction temperature was set at 60 ℃, and the stirring speed was set at 250 r min^{-1}. At the end of the reaction, the formed suspension was aged for 24 h, and then the residual Na_2CO_3 was removed by washing, and the resulting precursor powder $Ni_{1/6}Co_{1/6}Mn_{4/6}CO_3$ was finally collected by drying. The pristine LLO cathodes were synthesized using solid-phase lithiated carbonate precursors. The precursor with a molar ratio of 1:1.4 and the lithium source Li_2CO_3 were mixed well by ball milling, and the mixed powders were pretreated in air at 500 ℃ for 5 h and then calcined at 850 ℃ for 12 h. They were then cooled to room temperature in a furnace to obtain a pristine LLO cathode.

In order to synthesize brine-quenched LLO samples (LLOM for example), 102.564 g of $Mg(NO_3)_2$ was first dissolved in deionized water and ultrasonically stirred for 2 h until it was completely dissolved, and configured into 800 mL of 0.5 mol/L magnesium nitrate solution for use. Then, the molten state powder (200 g), which had been calcined at 850 ℃ for 12 h (without natural cooling), was rapidly immersed into the above $Mg(NO_3)_2$ solution for brine quenching under magnetic stirring and the reaction was stirred for 1 h at room temperature. Subsequently, the samples were then centrifuged, filtered, washed and dried under vacuum at 80 ℃ for 10 h. Finally, the dried samples were ground and sieved to obtain brine-quenched LLOM and stored in a sealed container. Similarly, the samples after quenching by immersion of the molten powders in $Al(NO_3)_3$, $Fe(NO_3)_3$, and $Sr(NO_3)_2$ solutions were labelled as LLOA, LLOF and LLOS, respectively. For comparison, we quenched the molten powders by

direct immersion in deionized water, referred to as LLODIW.

Materials characterizations.

X-ray diffraction (XRD, D8 Advance, Bruker AXS, λ= 1.5406 Å) with a Cu Kα radiation source operating at 40 kV and 40 mA was used to generate the crystal structure of the electrode material after cycling. The data were collected in 2θ with the value range of 10–90°. The microscopic morphology of secondary particles was examined using field emission scanning electron microscopy (FESEM, Hitachi S-4800) and focused ion beam-scanning electron microscope (FIB-SEM, FEI Helios Nanolab 600i). HAADF-STEM images and Electron energy loss spectroscopy (EELS) line scan spectra were obtained by using double spherical aberration-corrected Spectra 300 electron microscopes (Spectra 300, FEI) operated at 300 kV using a convergence semi-angle of 24.9 mrad for direct observations on atomic arrangements of all samples. EELS analysis was performed with a Gatan Image Filter (GIF Quantum 965, Gatan Inc.). The atomic composition of the primary particle was identified using EDX. Transmission electron microscopy (S/TEM, ThemoFisher Talos-F200x) was used to characterize HRTEM images of the changed electrodes after cycling. The surface elemental compositions of different electrodes before and after cycling were observed using X-ray photoelectron spectroscopy at 1.487 keV photoenergy (XPS, Kratos, Axis ultra DLD). The sample was transferred from the argon-filled glovebox to the XPS vacuum chamber using a sealed glass container. Depth profiling was carried out using Ar ion-beam sputtering at 5 keV, with data collected every 2 minutes for a total of 10 minutes. The depth profiles of element concentration were characterized by TOF-SIMS (TOF.SIMS 5–100) at 10^{-9} Torr. During the analysis, the samples before and after quenching were bombarded by pulsed 30 keV Bi beams, and the collection area was 50×50 μm^2. The graphitic peak in the C 1s spectra at 284.8 eV was used to calibrate the peak location of surface elements. The vibrational modes of chemical bonding on the surface of different electrode materials before and after cycling were investigated using a confocal Raman spectrometer (Raman, Renishaw, Renishaw inVia Reflex) and a 532 nm laser. Electron paramagnetic resonance (EPR, E500) spectra were collected on a Bruker X-band A200 computerized spectrometer with a

microwave frequency of 9.8 GHz (X band) and a microwave power of 2 mW. The field was modulated at a frequency of 100 KHz. Inductively coupled plasma optical emission spectrometry (ICP-OES, SPECTRO ARCOS II, SPECTRO) was used to analyze the elemental concentrations and compositions of different electrodes before and after modification.

Hard X-ray absorption spectroscopy (hXAS) experiments were carried out with transmission mode at beamline BL11B of the Shanghai Synchrotron Radiation Facility (SSRF) in Shanghai, China. The Athena software package[2] was used to process and fit the X-ray absorption near edge structure (XANES) and extended X-ray absorption fine structure (EXAFS) data. Soft X-ray absorption spectroscopy (sXAS) experiments were performed at beamline BL08U1-A of the Shanghai Synchrotron Radiation Facility (SSRF) at Shanghai, China. The total number of electrons emitted from the sample was counted in TEY mode at room temperature under ultrahigh vacuum (10^{-5}−10^{-6} Torr).

The SXAS spectra were recorded over a wide energy range from 520 to 562 eV covering energies well below and above sample absorptions. The normalization was performed following the established procedure:[3] (1) For I_0-normalization, the sample signal is divided by the incident intensity measured from the sample drain current from a freshly coated Au-mesh inserted into the beam path before the X-rays can impinge on the sample. (2) A linear, sloping background is removed by fitting a line to the flat low-energy region (from 520 to 524 eV) of the SXAS spectrum, i.e., at energies below any absorption peaks. (3) The spectrum is normalized by setting the flat low-energy region to zero and the postedge to unity (unit edge- jump). The photon energy selected for the postedge was 560 eV, again beyond the region of any absorption (peaks), though the normalization is insensitive to the exact value since this is sufficiently above any compound-specific resonances.

Variable-temperature in situ SXRD experiments and SXRD patterns were performed at the beamline BL14B of the Shanghai Synchrotron Radiation Facility (SSRF) at an X-ray wavelength of 0.6887 Å. During in-situ synthesis, the samples were first heated

to 500 ℃ at a rate of 5 ℃ min[-1], then maintained at 500 ℃ for a constant 40 min, and lastly cooled to room temperature of 25 ℃ at a rate of 10 ℃ min[-1].

Neutron powder diffraction (NPD) patterns were obtained at the GPDD beamline of China Spallation Neutron Source (CSNS). The joint refinements using NPD and SXRD data were performed by the GSAS-II program based on the Rietveld method.[4] After cycling, the cycled electrode material was removed from the cell and scraped off the Al current collector. Following a thorough cleaning with pure DMC solvent to eliminate any remaining salts, the electrode material was vacuum-dried and gently ground in an agate mortar and pestle to prevent excessive particle aggregation.

DFT Calculation

The first-principles calculations were performed within the density functional theory framework by using the projector augmented wave (PAW) method, as implemented in the Vienna ab initio simulation package (VASP),[5, 6] which is based on density functional theory (DFT). We adopted the spin-polarized generalized gradient approximation (GGA)+U method with Perdew-Burke Ernzerhof (PBE) exchange-correlation function for formation energy, and Meta-GGA for density of state, where the U values were 4.9, 6.0 and 4.91 eV for Mn, Ni and Co in the $Li_{33}Ni_3Co_3Mn_{15}O_{54}$ system, respectively.[7, 8] The energy and force convergence values were chosen as 10^{-5} eV and 0.03 eV $Å^{-1}$, respectively. The Kohn-Sham orbitals were expanded in plane waves with a kinetic energy cut-off of 500 eV. The Brillouin zone integration and k-point sampling were performed with a Monk Horst-Pack scheme of $2 \times 2 \times 2$ grid with Γ symmetry for all calculations.[9] The formation energy of M (Sr, Mg, Al, Fe) doped and oxygen vacancy formation in LLO was calculated based on the total energy of LLO by the reported approach.[10, 11]

The formation energies (E_{dop}) of each doping site and doping element were calculated. Taking the Li site occupied by Mg as an example, E_{dop} is described by the following equations:

$$E_{dop} = E(Li_{32}Ni_3Co_3Mn_{15}MgO_{54}) + E(Li) - E(Li_{33}Ni_3Co_3Mn_{15}O_{54}) - E(Mg)$$
(1)

Where $E(Li_{32}Ni_3Co_3Mn_{15}MgO_{54})$ and $E(Li_{33}Ni_3Co_3Mn_{15}O_{54})$ are the total energy of the system before and after one Li site occupied by Mg, respectively. $E(Li)$ and

$E(\text{Mg})$ are the energy of Li and Mg single atoms, respectively.

The oxygen vacancy formation energy (E_{ov}) was calculated by the following equations:

$$E_{ov} = E(\text{Li}_{32}\text{Ni}_3\text{Co}_3\text{Mn}_{15}\text{MgO}_{53}) + 1/2E(\text{O}_2) - E(\text{Li}_{32}\text{Ni}_3\text{Co}_3\text{Mn}_{15}\text{MgO}_{54})$$
(2)

Where $E(\text{Li}_{32}\text{Ni}_3\text{Co}_3\text{Mn}_{15}\text{MgO}_{54})$ and $E(\text{Li}_{32}\text{Ni}_3\text{Co}_3\text{Mn}_{15}\text{MgO}_{53})$ are the total energy of the system with and without oxygen vacancy and $E(\text{O}_2)$ is the chemical potential of O_2.

Electrochemical measurements

The cathode materials, Super-P (SP) and polyvinylidene fluoride (PVDF) were mixed uniformly in N-methyl-2-pyrrolidone (NMP) with a mass ratio of 8: 1: 1. The slurry was spread on aluminum foil with a certain thickness and dried at 80 $^{\circ}$C for 12 hours. The active material loading of the cathode electrode is 6–7 mg cm^{-2}. 1 M LiPF$_6$ dissolved in ethylene carbonate and diethyl methyl carbonate with a volume ratio of 3: 7. The CR2032 coin cells were assembled in an Argon-filled glove box, using Celgard 2502 as the separator and Li metal as the anode. The galvanostatic charge-discharge cycling of cells was carried out in the voltage window of 2.0–4.8 V (*vs.* Li$^+$/Li^0) using the LAND-CT2001A battery testing system at room temperature. The cells were first activated at the current density of 0.1 C (1 C= 250 mAh g^{-1}). The electrochemical impedance spectroscopy (EIS) was carried out using a Solartron Analytical system (Solatron, 1470E) over a frequency range of 100 kHz to 0.1 Hz. The galvanostatic intermittent titration technique (GITT) was performed with 20 min charging and 2 h relaxation. The following simplified formula was used to compute the Li$^+$ diffusion coefficient:

$$D_{Li^+} = \frac{4}{\pi\tau}\left(\frac{mV_M}{MS}\right)^2\left(\frac{\Delta E_S}{\Delta E_\tau}\right)^2$$

The pouch cells were assembled with LLOM and graphite as cathode and anode, respectively. Wherein, the cathode is consisted of active materials (92%), PVDF (2.0%), CNTs (1.0%), KS-6 (2.16%), SP (2.0%) and SWCNTs (0.84%), and the slurry was spread on aluminum foil. The anode has consisted of graphite (93.5%), KS-6 (1.0%), SP (1.0%), SWCNTs (0.5%), styrene-butadiene rubber (SBR, 2.3%) and aqueous binder (CMC, 1.7%), and the slurry was spread on copper foil. The N/P ratio

was settled to be 1.07. The 1.6 Ah pouch cell is assembled in the drying room (30% RH, 25 $^{\circ}$C). An electrolyte of 3.5 g Ah^{-1} was injected into an argon glovebox. The galvanostatic charge-discharge cycling of pouch cells was performed at the voltage window of 2.0–4.55 V (*vs.* Li^{+}/Li^{0}) using the NEWARE-CT4008 battery testing system.

Operando **DEMS measurements**

Operando electrochemical mass spectroscopy (DEMS, Zero Dew Instruments, Shanghai) can be used to monitor online the gas production of the electrode material during the first charge/discharge process. Gas chromatography (GC, Agilent) was used to analyze the composition of the gases (mainly O_2 and CO_2) produced after cycling, and the battery type used for the DEMS test was a Swagelok-type battery. The test procedure consisted of connecting the assembled Swagelok-type cell to a mass spectrometer and an electrochemical workstation (Solatron, 1470E), and purging the cell with He gas at a rate of 0.5 ml min^{-1} for 6 h to remove airborne O_2 and CO_2 from the test. Subsequently, the electrochemical workstation was activated and the test was performed in the range of 2.0–4.8 V at a multiplicity of 0.1 C. He gas was continuously passed through the Swagelok-type cell to bring the gas inside the Swagelok-type cell into the mass spectrometer continuously for MS analysis. In the data in the mass spectrometer, the mass signal of the gas is the vertical coordinate and time is the horizontal coordinate, and the temporal resolution of the ion current intensity was optimized by selectively scanning the *m/z* = 44 and 32 signals.
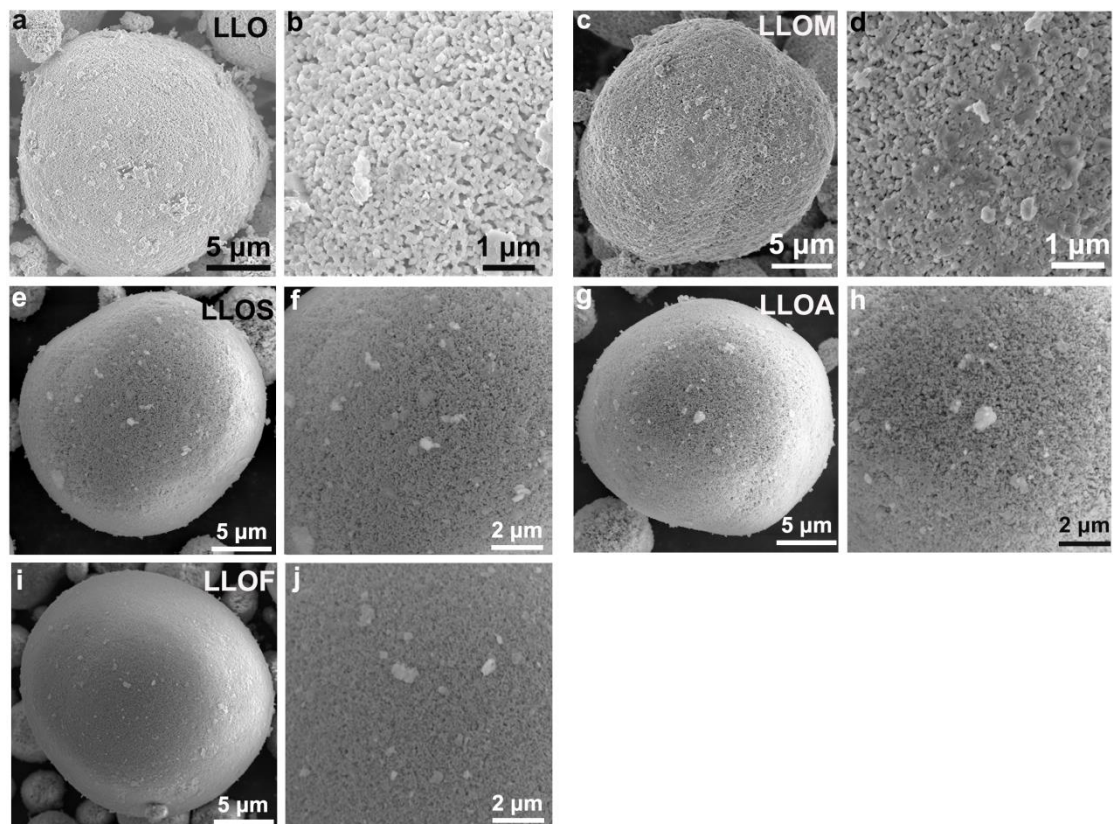
Supplementary Fig.

Fig. S1 Morphology of synthesized materials. a, b) SEM images of LLO at low magnification (a) and high magnification (b). c, d) SEM images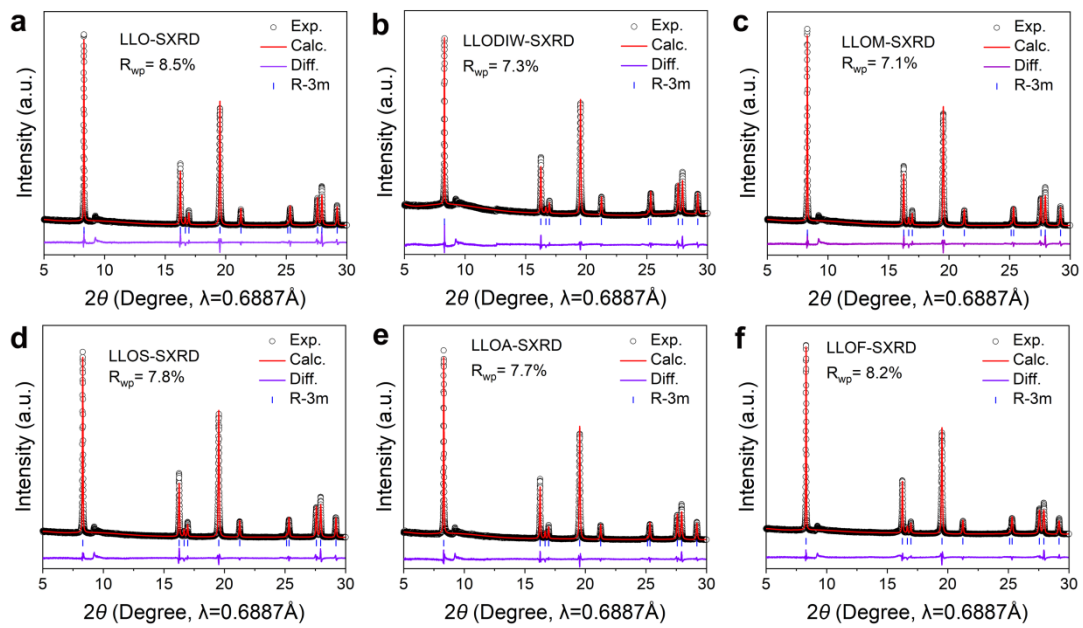 of LLOM at low magnification (c) and high magnification (d). e, f) SEM images of LLOS at low magnification (e) and high magnification (f). g, h) SEM images of LLOA at low magnification (g) and high magnification (h). i, j) SEM images of LLOF at low magnification (i) and high magnification (j)

Fig. S2 Rietveld refinement results of the X-ray diffraction patterns of LLOs and quenched samples.
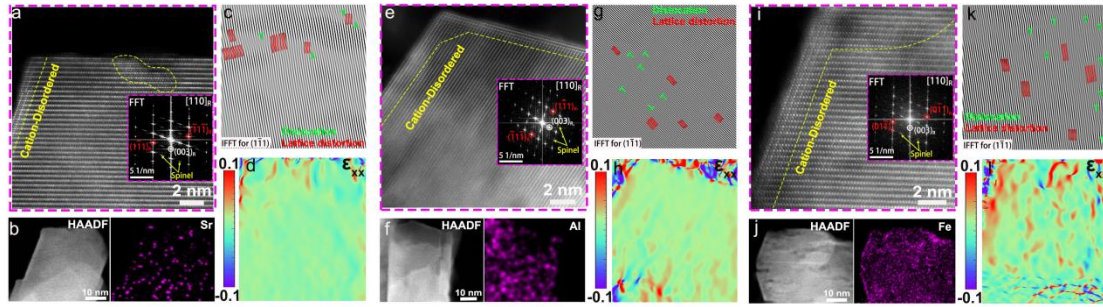
Fig. S3 Atomic-scale structural characterizations and analysis of the LLOS, LLOA and LLOF. a) Atomic-resolution HADDF-STEM image with the FFT pattern of the interlayer structure reflection projected along $[110]_R$ rhombohedral direction for LLOS cathodes. b) STEM-HAADF images and the corresponding EDX mapping of the LLOS cathode. c) Inverse fast Fourier transformation (IFFT) of (1 −1 1) spots in (a). d) The corresponding geometric phase analysis (GPA) of the LLOS cathode used to show the ε_{xx} strain observed in (a). e) Atomic-resolution HADDF-STEM images with the FFT pattern of the interlayer structure reflection projected along $[110]_R$ rhombohedral direction for LLOA cathodes. f) STEM-HAADF images and the corresponding EDX mapping of the LLOA cathode. g) Inverse fast Fourier transformation (IFFT) of (1 −1 1) spots in (e). h) The corresponding geometric phase analysis (GPA) of the LLOA cathode used to show the ε_{xx} strain observed in (e). i) Atomic-resolution HADDF-STEM images with the FFT pattern of the interlayer structure reflection projected along $[110]_R$ rhombohedral direction for LLOF cathodes. j) STEM-HAADF images and the corresponding EDX mapping of the LLOF cathode. k) Inverse fast Fourier transformation (IFFT) of (1 −1 1) spots in (i). l) The corresponding geometric phase analysis (GPA) of the LLOF cathode used to show the ε_{xx} strain observed in (i).
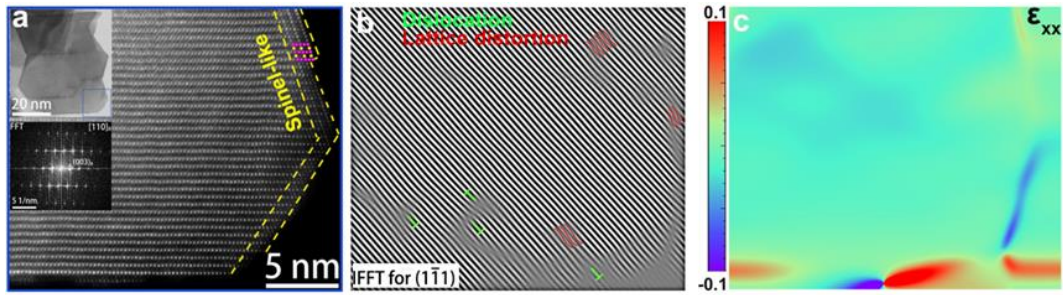
Fig. S4 Atomic-scale structural characterizations and analysis of the LLODIW. a) Atomic-resolution HADDF-STEM image with the FFT pattern of the interlayer structure reflection projected along $[110]_R$ rhombohedral direction for LLODIW cathodes. b) Inverse fast Fourier transformation (IFFT) of $(1\ -1\ 1)$ spots in (a). c) The corresponding geometric phase analysis (GPA) of the LLODIW cathode used to show the ε_{xx} strain observed in (a).
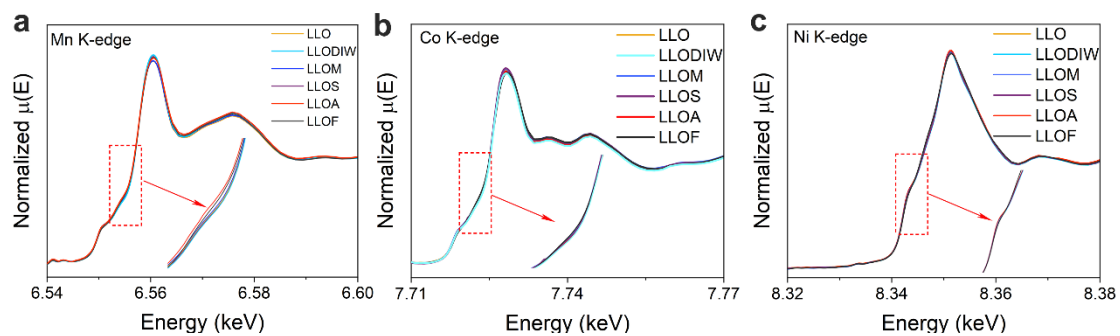
Fig. S5 Structural characterization of LLO and quenched samples. a) K-edge XANES spectra of Mn for LLO and quenched samples. b) K-edge XANES spectra of Co for LLO and quenched samples. c) K-edge XANES spectra of Ni for LLO and quenched samples.
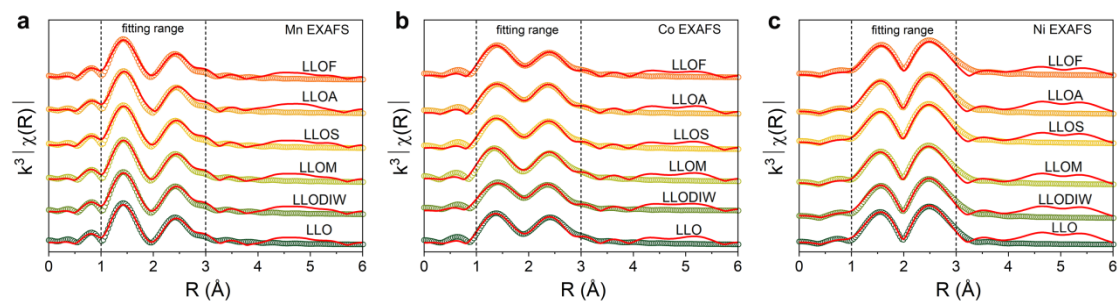
Fig. S6 TM EXAFS fitting patterns of LLO and quenched samples. Only the first two coordination shells were fitted. a) Mn EXAFS fitting patterns of LLO and quenched samples. Only the first two coordination shells were fitted. b) Co EXAFS fitting patterns of LLO and quenched samples. Only the first two coordination shells were fitted. c) Ni EXAFS fitting patterns of LLO and quenched samples. Only the first two coordination shells were fitted.
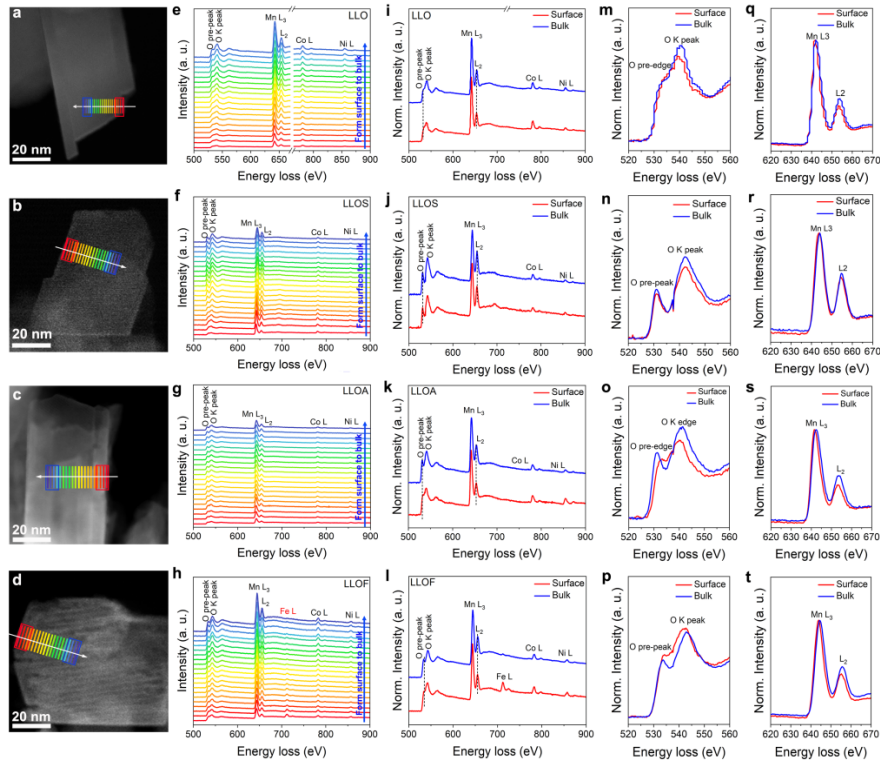
Fig. S7 Relative surface and bulk composition changes for the LLO, LLOS, LLOA and LLOF. a) STEM image and the EELS line scanning pathway of LLO cathode. b) STEM image and the EELS line scanning pathway of LLOS cathode. c) STEM image and the EELS line scanning pathway of LLOA cathode. d) STEM image and the EELS line scanning pathway of LLOF cathode. e) EELS spectrum profiles of LLO cathode from the particle surface to the bulk as marked by the horizontal solid lines with the same colour as in (a). f) EELS spectrum profiles of LLOS cathode from the particle surface to the bulk as marked by the horizontal solid lines with the same colour as in (b). g) EELS spectrum profiles of LLOA cathode from the particle surface to the bulk as marked by the horizontal solid lines with the same colour as in (c). h) EELS spectrum profiles of LLOF cathode from the particle surface to the bulk as marked by the horizontal solid lines with the same colour as in (d). i) EELS spectrum profiles of LLO and LLOM from the particle surface (red) and bulk (blue). j) EELS spectrum profiles of LLO and LLOS from the particle surface (red) and bulk (blue). k) EELS spectrum profiles of LLO and LLOA from the particle surface (red) and bulk (blue). l) EELS spectrum profiles of LLO and LLOF from the particle surface (red) and bulk (blue). m) Detailed comparisons of the O K edges of the

particle surface and the bulk of LLO particle. n) Detailed comparisons of the O K edges of the particle surface and the bulk of LLOS particle. o) Detailed comparisons of the O K edges of the particle surface and the bulk of LLOA particle. p) Detailed comparisons of the O K edges of the particle surface and the bulk of LLOF particle. q) Detailed comparisons of the Mn L edges of the particle surface and the bulk of LLO particle. r) Detailed comparisons of the Mn L edges of the particle surface and the bulk of LLOS particle. s) Detailed comparisons of the Mn L edges of the particle surface and the bulk of LLOA particle. t) Detailed comparisons of the Mn L edges of the particle surface and the bulk of LLOF particle.
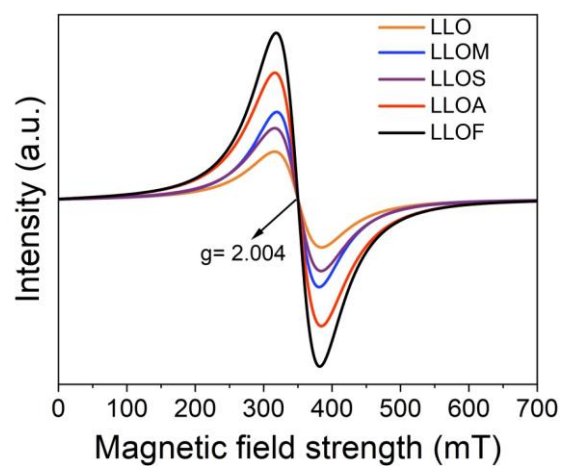
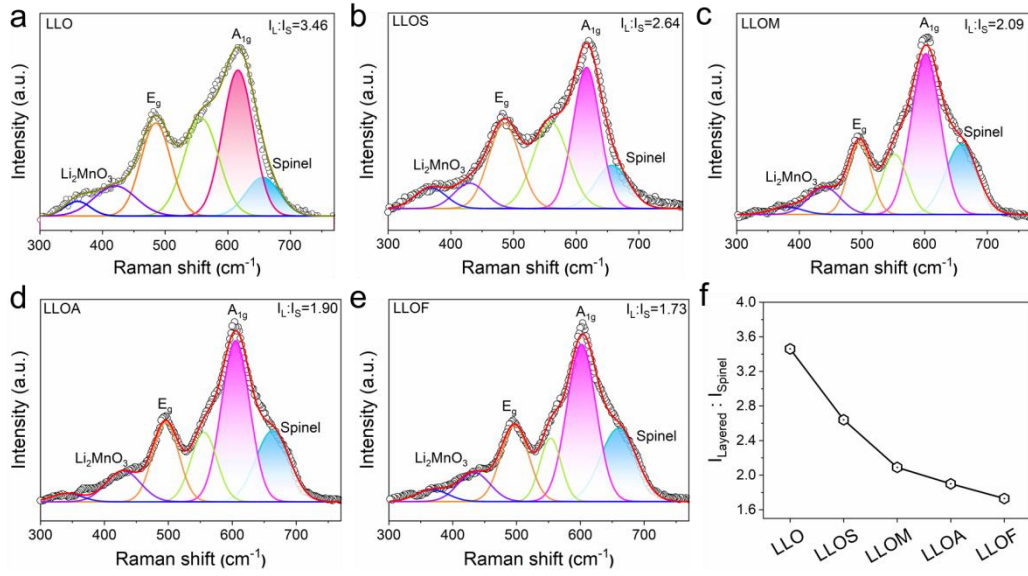**Fig. S8** Electron paramagnetic resonance (EPR) analysis was performed on LLO and quenched samples.

Fig. S9 Raman spectroscopy was performed on LLO and quenched samples. a-f Raman spectra of LLO, LLOS, LLOM, LLOA and LLOF samples and their fitting results.
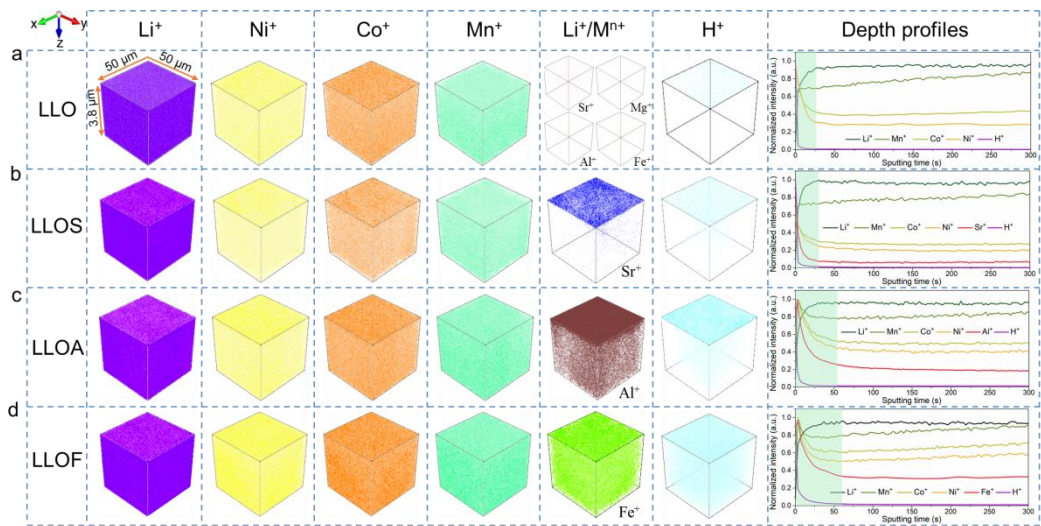
Fig. S10 a-d) TOF-SIMS depth curves and three-dimension depth images of the Li^+, Ni^+, Co^+, Mn^+, M^{n+} and H^+ species in LLO (a), LLOS (b), LLOA (c) and LLOF (d) particles.
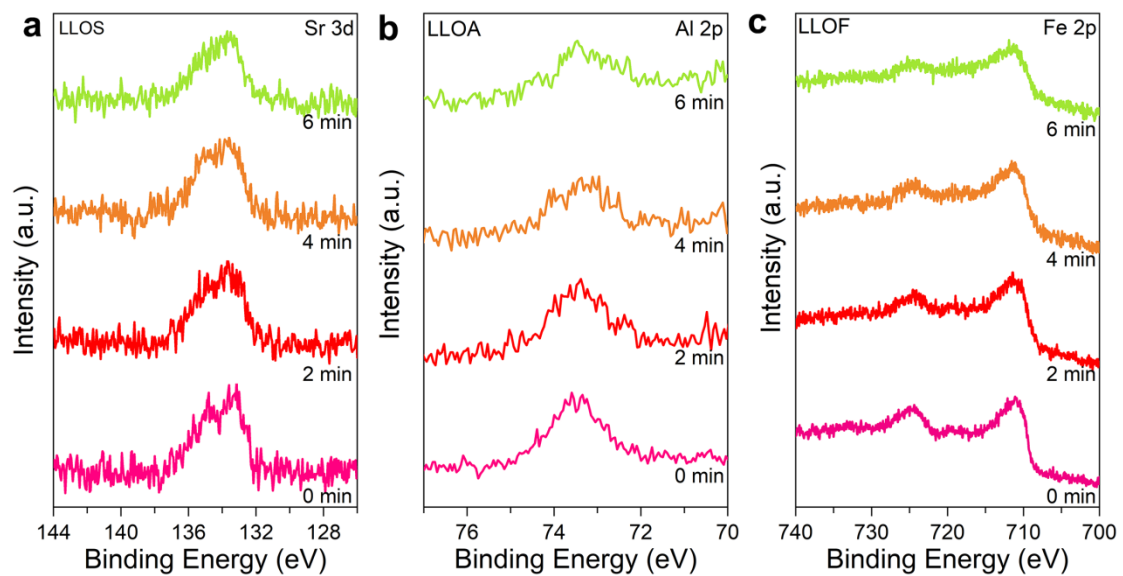
Fig. S11 Surface analyses of LLOS, LLOA and LLOF samples. a) XPS spectra for Sr 3d of LLOS at different etching levels. b) XPS spectra for Al 2p of LLOA at different etching levels. c) XPS spectra for Fe 2p of LLOF at different etching levels.
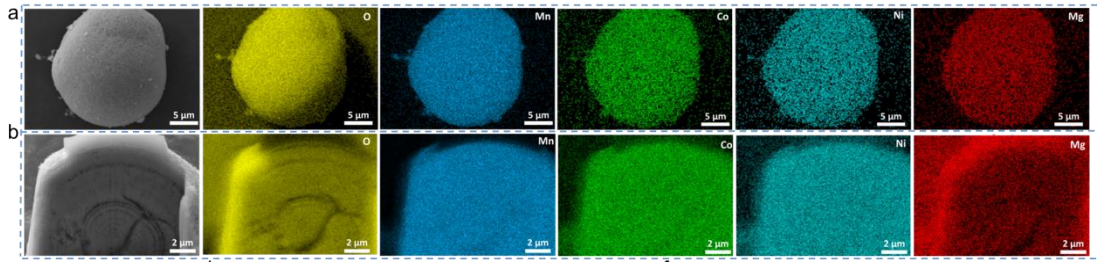
Fig. S12 a) EDS elemental distribution mapping of the surface of LLOM secondary particles before cross-section treatment. b) SEM images of the cross-sections of the LLOM and corresponding EDS elemental distribution mapping.

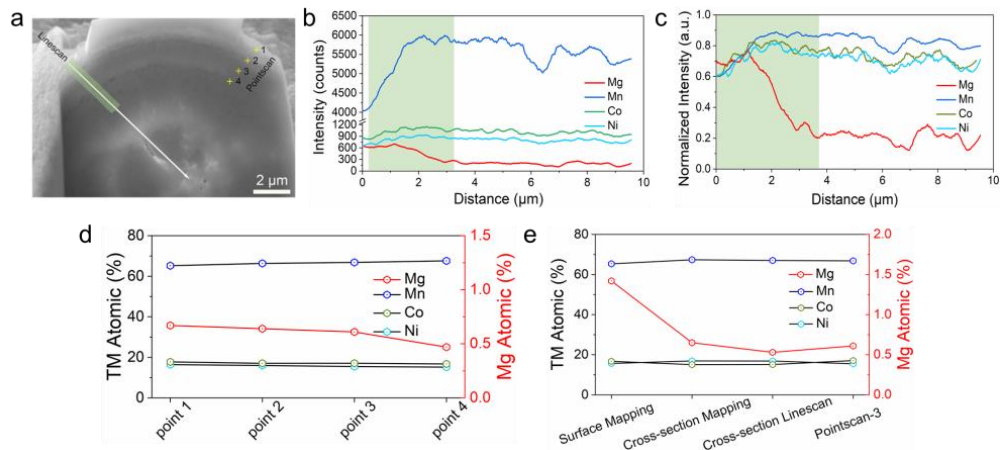**Fig. S13** a) SEM images of LLOM cross sections. b) Line-scan of the corresponding EDS elements of the LLOM section. c) Linescan normalized signal images of the corresponding EDS elements of the LLOM cross-section. d) b) A pointscan of the corresponding EDS element of the LLOM section. e) Comparison of the corresponding Mapping, linescan and pointscan elemental contents of surfaces and cross sections.

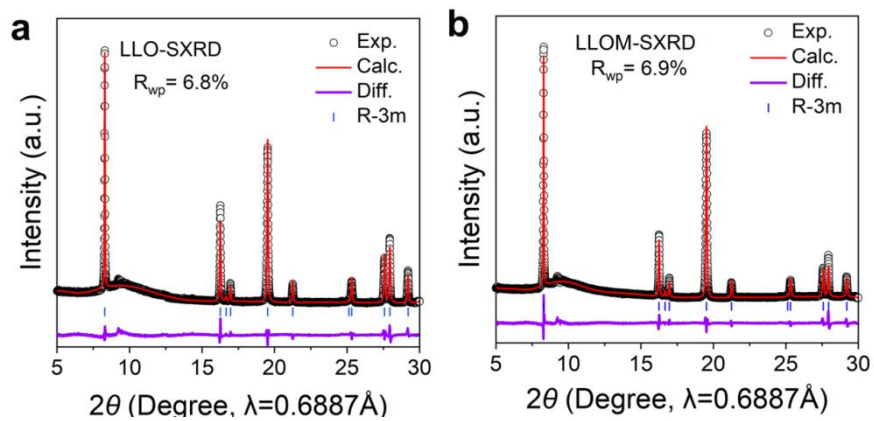**Fig. S14** a, b) The Joint Reitveld refinement patterns of SXRD for LLO (a) and LLOM (b).
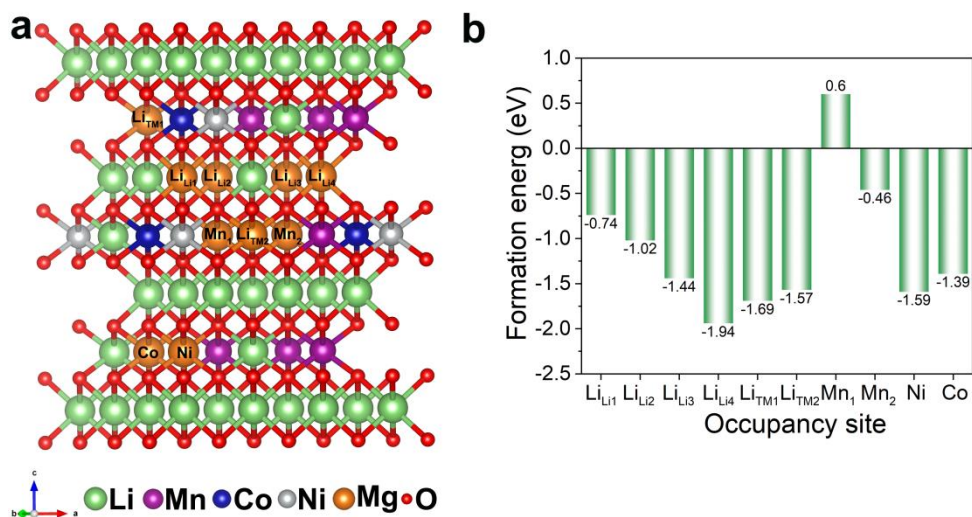
Fig. S15 Schematic diagram of the representative occupancy sites for Mg atom a), and the corresponding formation energies b).

Fig. S16. Schematic diagrams showing the different occupation sites of Mg atom in the lattice.
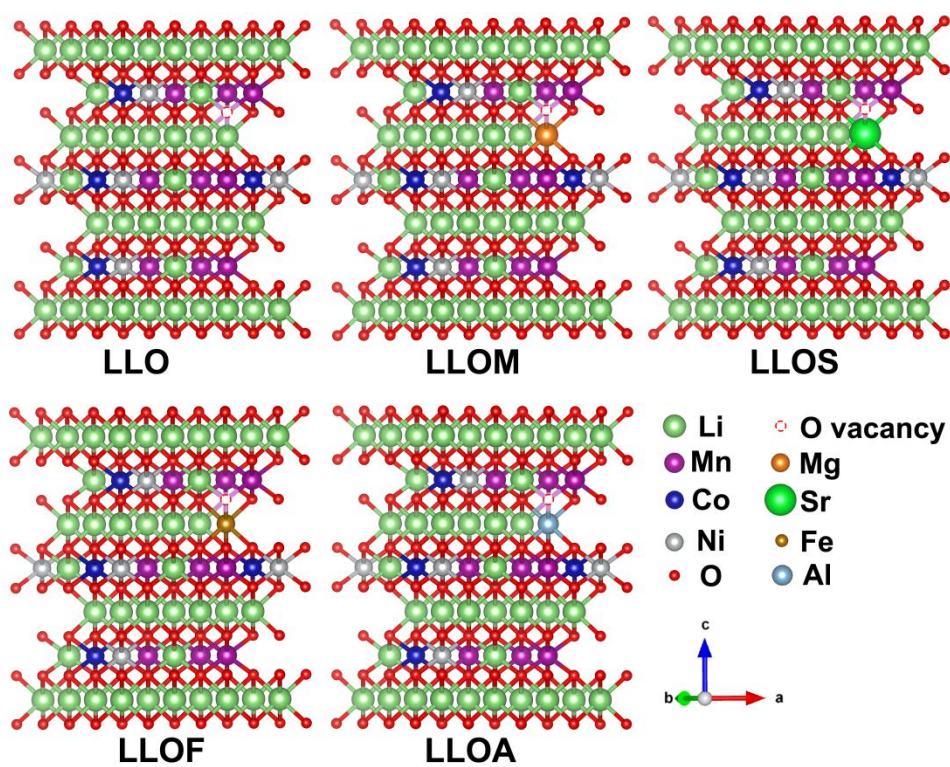
Fig. S17 Structural illustration of pristine LLO brine quenched samples for DFT calculations.
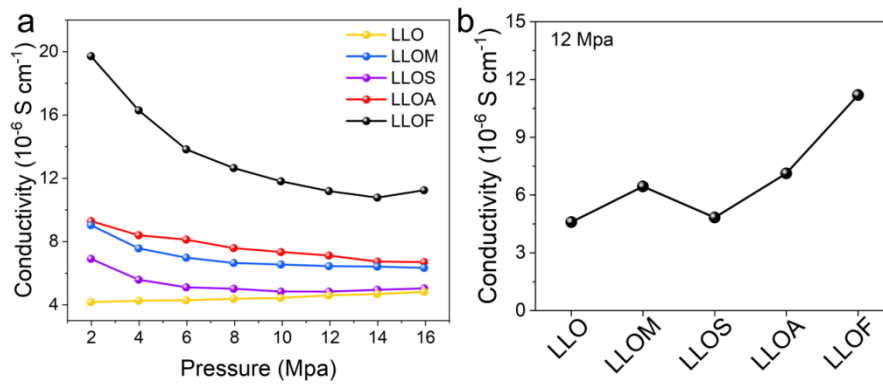
Fig. S18 a) Electrical conductivity of LLO, LLOM, LLOS, LLOA and LLOF samples as a function of pressure. b) Conductivity of different samples at a pressure of 12 MPa.
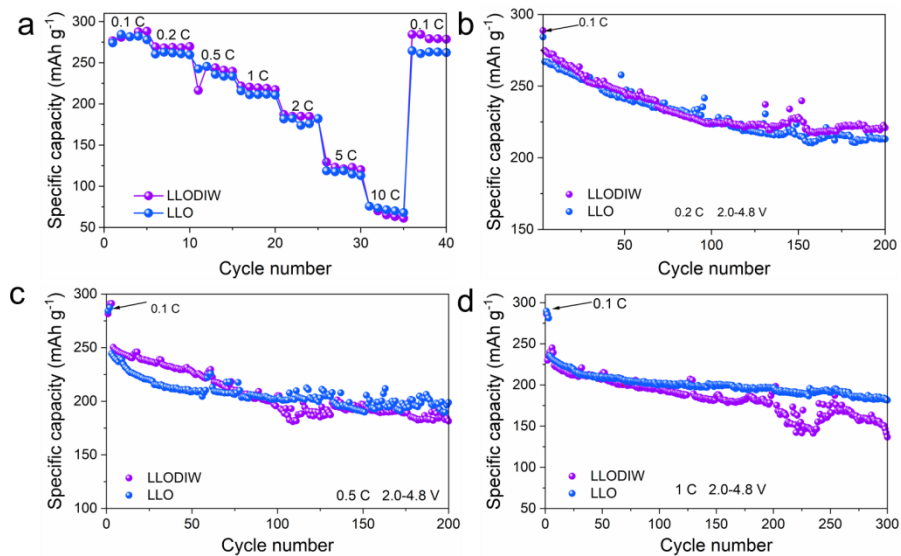
Fig. S19 Electrochemical properties of synthetic materials (LLODIW) after quenching in deionized water. a) Discharge-rate capacity of LLO and LLODIW. b) Cycling performance of LLO and LLODIW material at 0.2 C-rate after three form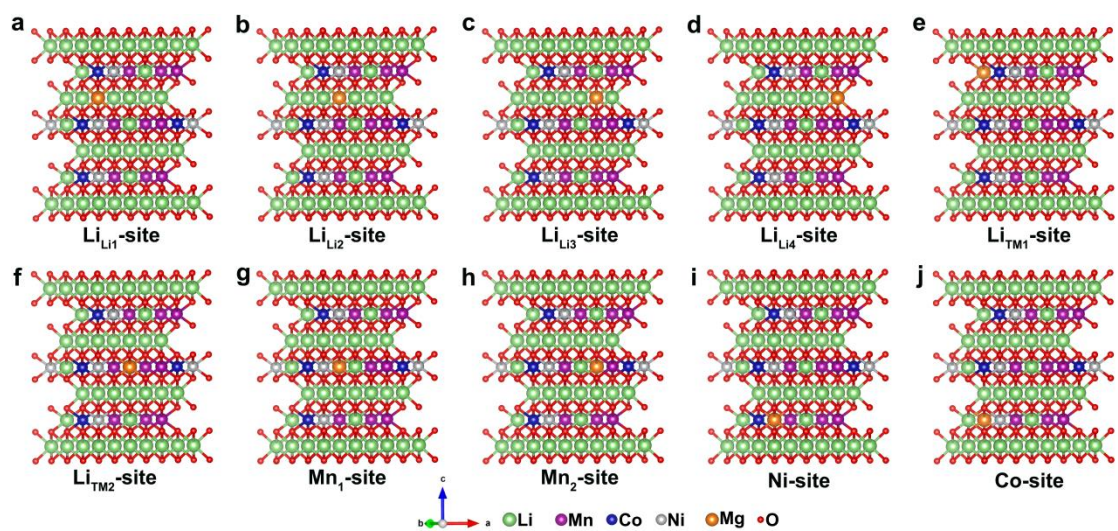ation cycles at 0.1 C-rate at room temperature. c) Cycling performance of LLO and LLODIW material at 0.5 C-rate after three formation cycles at 0.1 C-rate at room temperature. d) Cycling performance of LLO and LLODIW material at 1.0 C-rate after three formation cycles at 0.1 C-rate at room temperature.
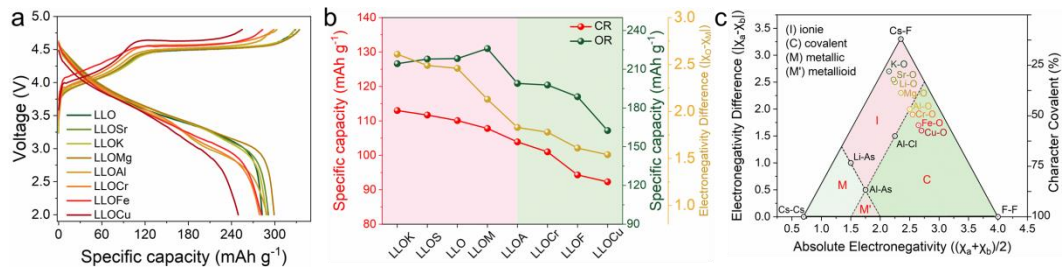
Fig. S20 a) Comparison of the initial charge-discharge curves of samples after different brine quench at 0.1 C. b) Comparison of the relationship between the charge capacity distribution and the electronegativity of M^{n+} ions in samples after quenching in different brines. c) Schematic diagram of Jensen's Quantitative Triangle[12] showing the classification of bonding types based on average electronegativities and electronegativity differences.
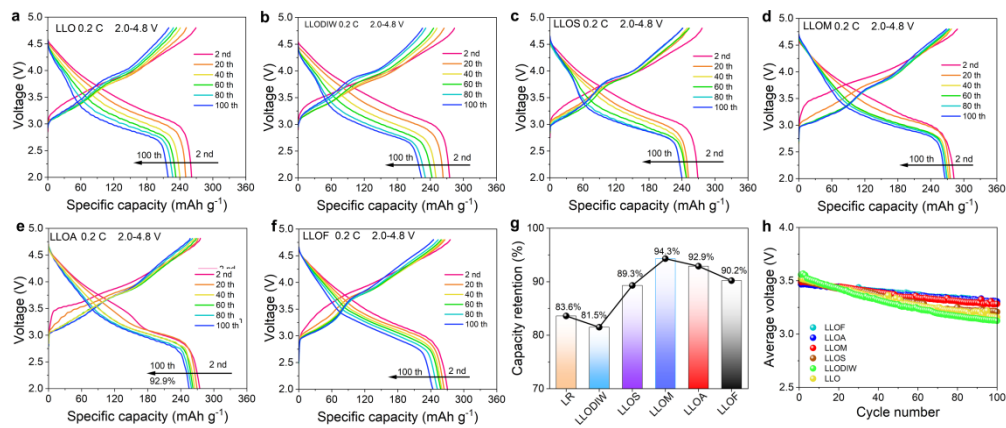
Fig. S21 Electrochemical properties of LLO and quenched materials. a-f) Discharge plots of the LLO and quenched materials at 0.2 C-rate cycled between 2.0 and 4.8 V. g) Discharge capacity retention of r LLO and quenched samples cycled 100 times at 0.2 C. h) Voltage decay of LLO and quench material at 0.2 C rate for 100 cycles.
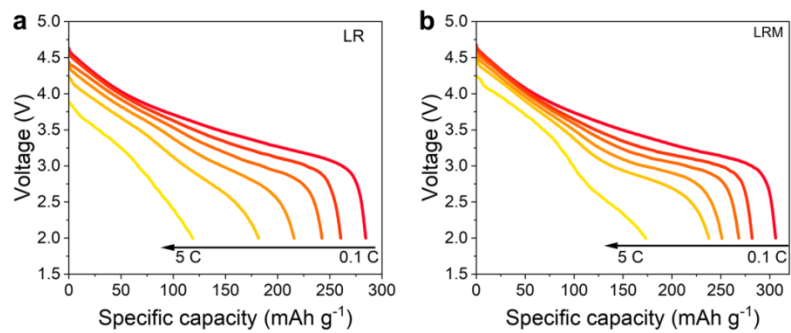
Fig. S22 Rate performance of LLO and LLOM. a, b) Discharge plots of LLO (a) and LLOM cathodes (b) at different rates.
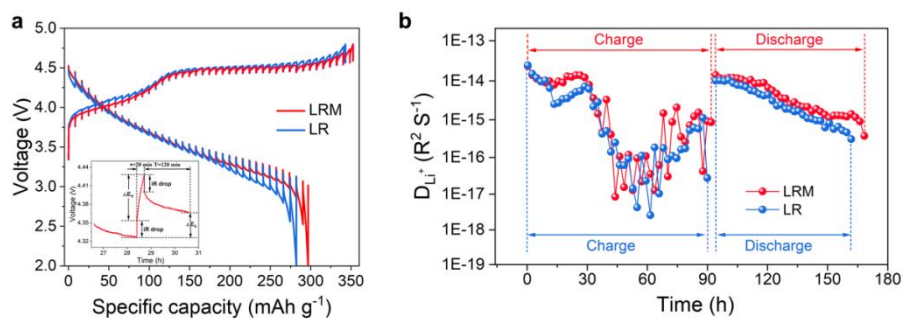
Fig. S23 GITT and in situ EIS test of LLO and LLOM. a) GITT test voltage profiles for LLO and LLOM electrodes. The duration of pulse current is 20 min, and the interval is 120 min as shown in the bottom insert Fig.. b) The evolution of D_{Li}^{+} according to the GITT data.
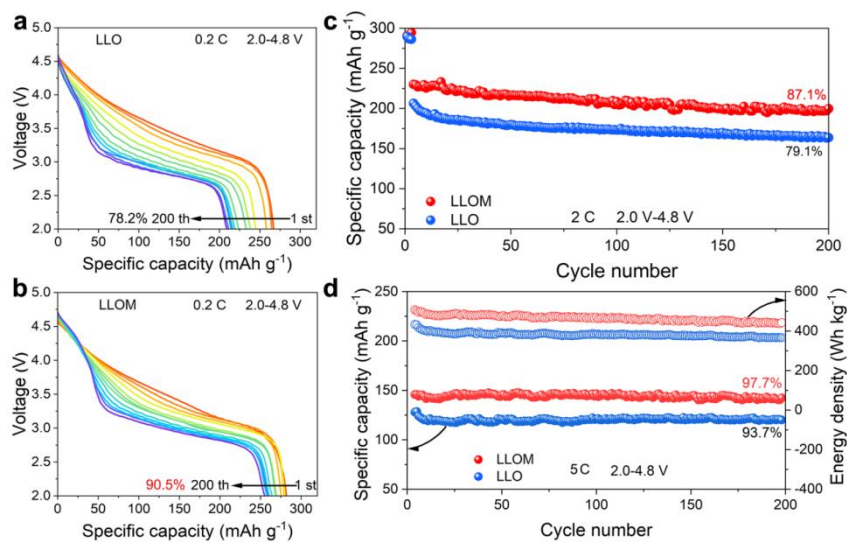
Fig. S24 Electrochemical properties of LLO and LLOM. a, b) Discharge plots of LLO a) and LLOM cathodes b) at 0.2 C-rate cycled between 2.0–4.8 V. c) Cycling performance of LLO and LLOM cathodes during 300 cycles at 2.0 C-rate and 25 ℃. d) Cycling performance of LLO and LLOM cathodes during 200 cycles at 5.0 C-rate and 25 ℃.
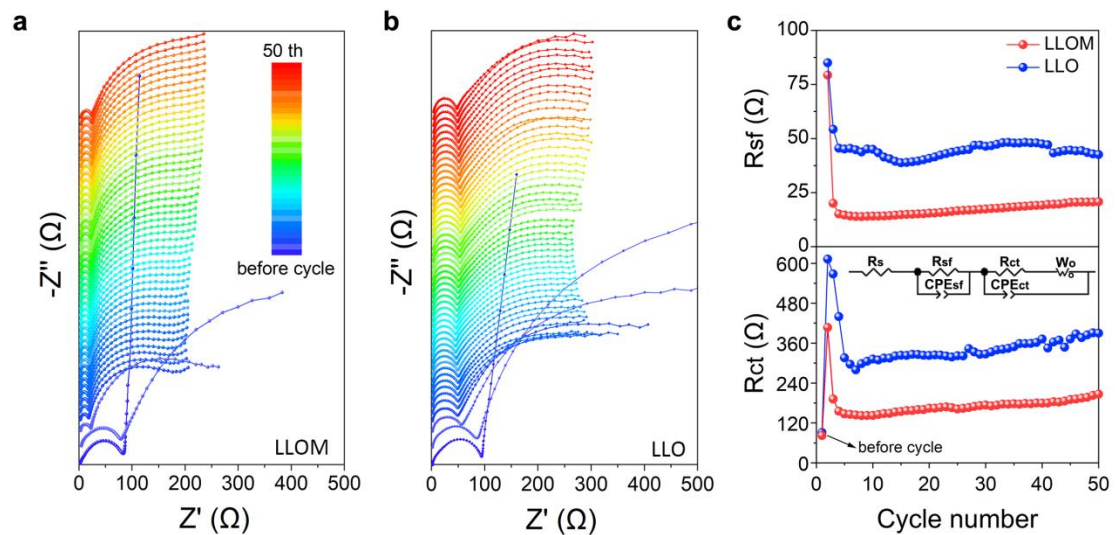
Fig. S25 In situ EIS test of LLO and LLOM. a) In situ EIS Nyquist plot of the LLO electrode during 50 cycles. b) In situ EIS Nyquist plot of the LLOM electrode during 50 cycles. Nyquist plots of the cells with the LLO and LLOM after initially charged to 4.8 V at 0.1 C-rate and rested at 1 h. c) Evolution of Rsf (top) and Rct (bottom) in 50 cycles of LLO and LLOM, which was simulated from EIS Nyquist plots in (a) and (b).
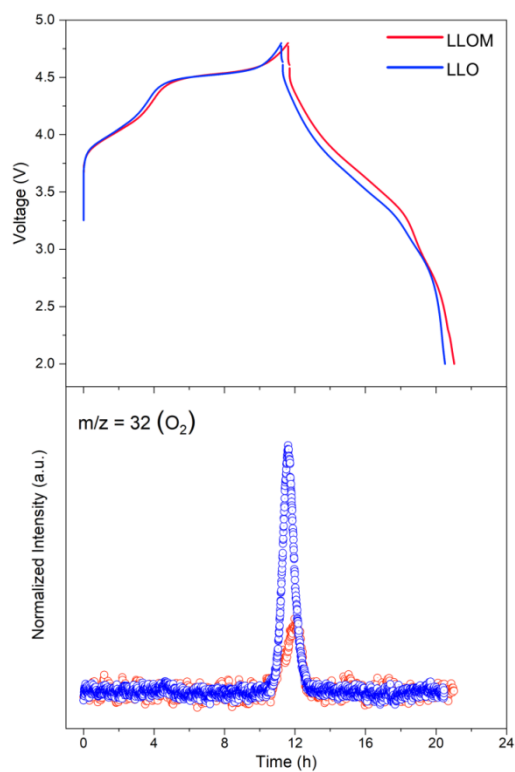
Fig. S26 Operando differential electrochemical mass spectroscopy. Initial cycle charge-discharge profile (top) and the normalized intensity measured by DEMS (bottom) for Oxygen gas of the LLO and LLOM electrode.
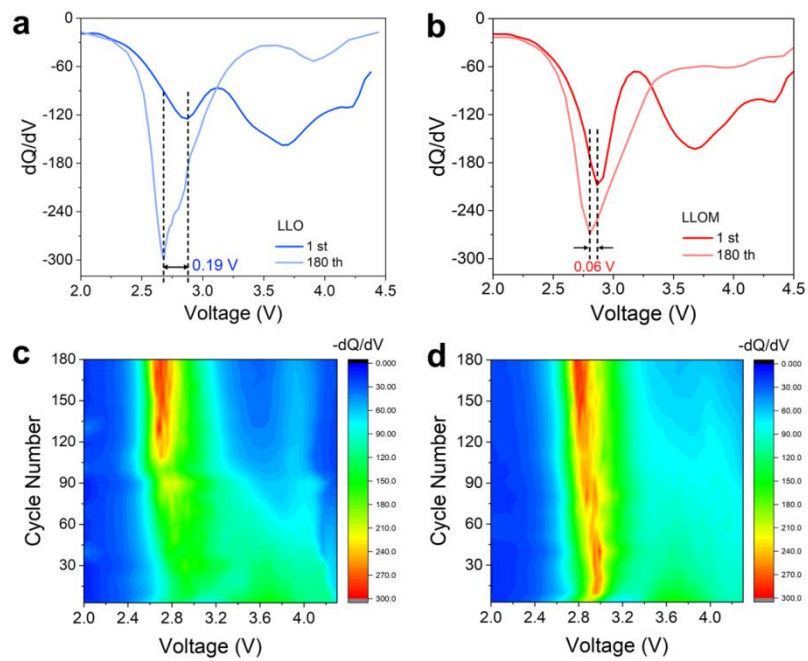
Fig. S27 dQ/dV curves for LLO and LLOM electrodes. a) The corresponding dQ/dV curves of LLO electrode after the initial and 180 cycles. b) The corresponding dQ/dV curves of LLOM electrode after the initial and 180 cycles. c, d) Differential discharge capacity curves of (c) LLO and (d) LLOM electrodes obtained from the discharge curves every ten cycles during the cycling tests.
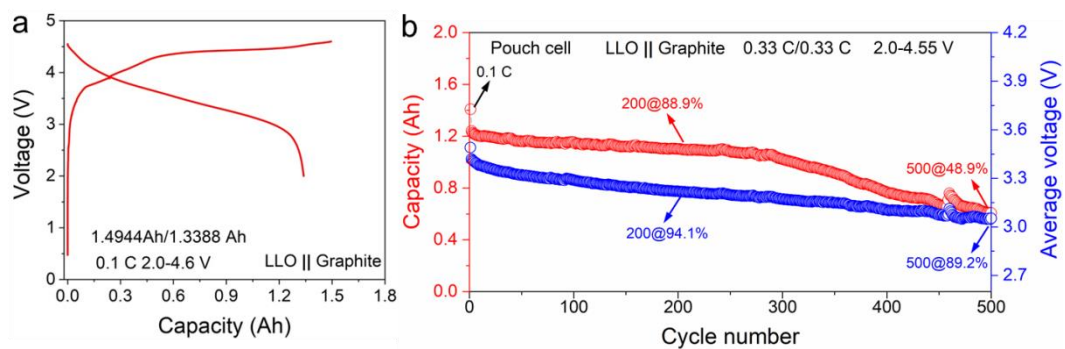
Fig. S28 a) Charge-discharge profiles of pristine LLO‖Graphite pouch cell in the window of 2.0–4.6 V. b) Cycling performance of LLO‖Graphite pouch cell at 0.33 C and 2.0–4.55 V (equal to 4.6 V vs Li/Li$^+$).
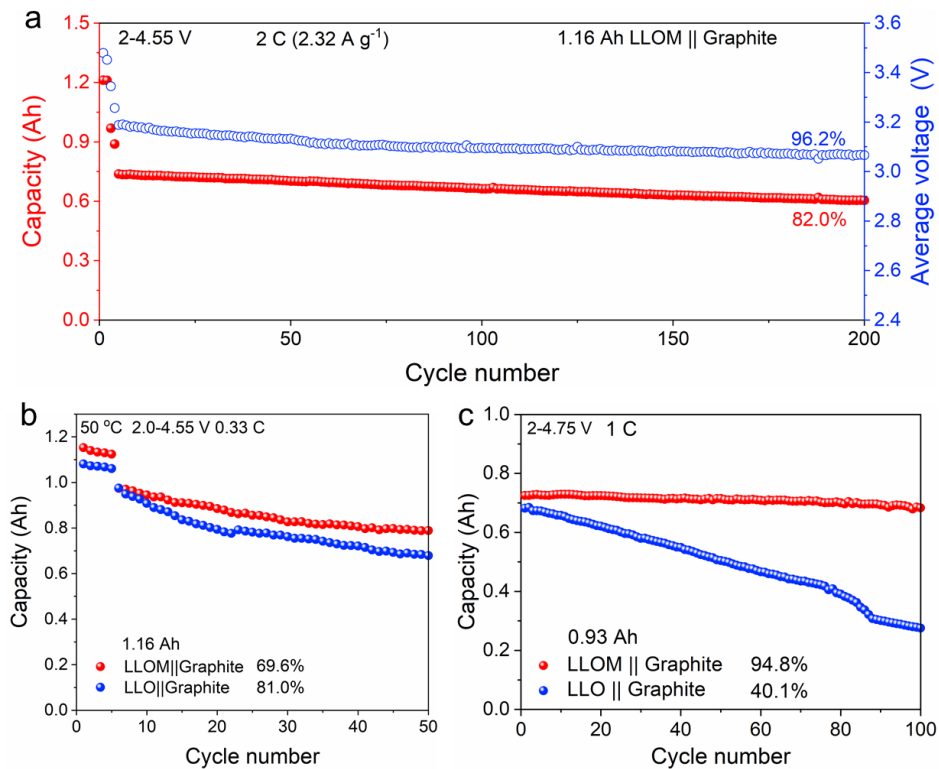
Fig. S29 a) The fast charge cyclic stability of the 1.16Ah LLOM‖Graphite pouch full cell at 2 C and 2.0–4.55 V (equal to 4.6 V vs Li/Li⁺). b) The high-temperature cycle performance of 1.16 Ah LLO‖Graphite and LLOM‖Graphite pouch cell at 0.33 C and 50 °C within 2.0–4.55 V (equal to 4.6 V vs Li/Li⁺) and 50 °C. c) The high voltage cycling performance of LLOM‖Graphite and LLO‖Graphite pouch cell at 1 C and 2.0–4.75 V (equal to 4.8 V vs Li/Li⁺).
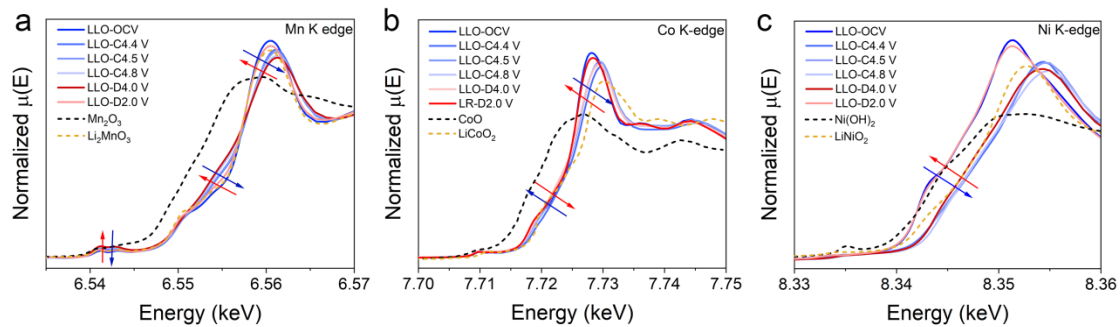
Fig. S30 Charge compensation mechanisms. a-c) The normalized Mn (a), Ni (b) and Co (c) K-edge spectra of LLO at different states of charge.
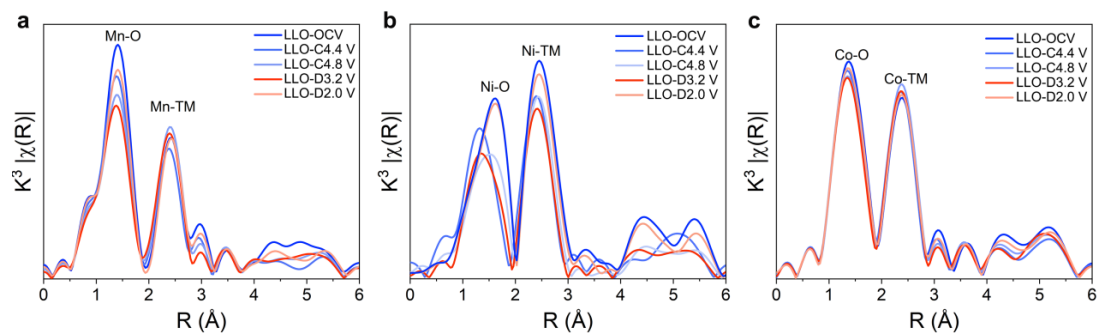
Fig. S31 Detection of TM (Ni, Co, Mn) coordination environments of LLO electrodes at different voltage states. a) K-edge EXAFS spectra of Mn for LLO samples during the initial charge-discharge. b) K-edge EXAFS spectra of Ni for LLO samples during the initial charge-discharge. c) K-edge EXAFS spectra of Co for LLO samples during the initial charge-discharge.
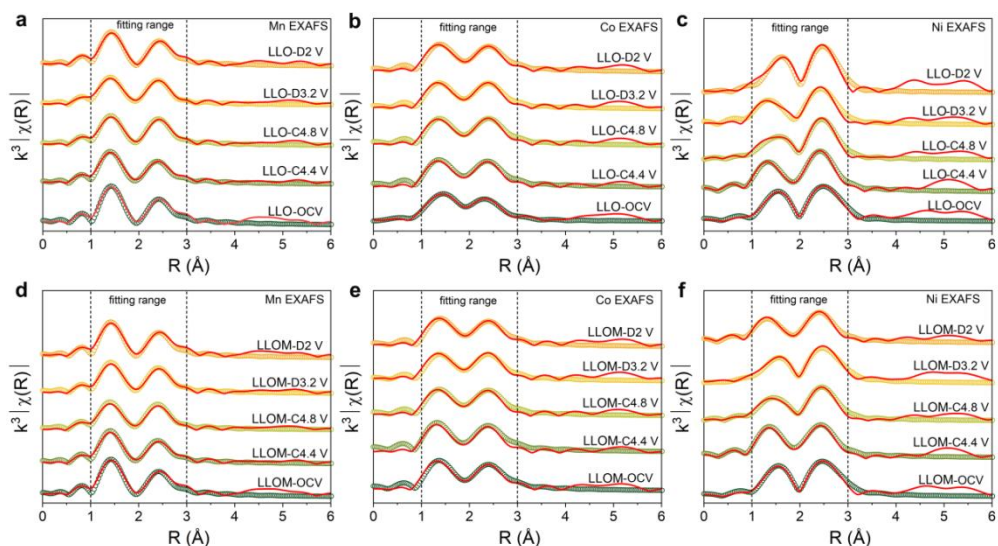
Fig. S32 TM EXAFS fitting patterns of the cycled LLO and LLOM samples. Only the first two coordination shells were fitted. a, d) The ex-situ Mn radial distribution function data (circles) and fitting curves (lines) for LLO (a) and LLOM (d). b, e) The ex-situ Co radial distribution function data (circles) and fitting curves (lines) for LLO (b) and LLOM (e). c, f) The ex-situ Ni radial distribution function data (circles) and fitting curves (lines) for LLO (c) and LLOM (f).
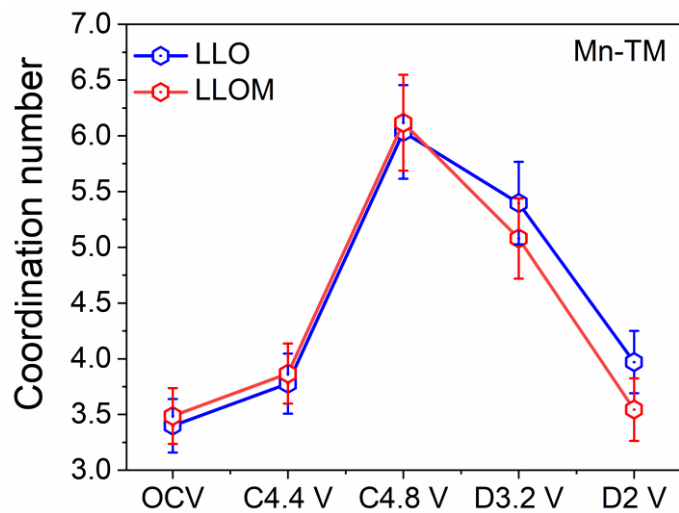
Figure S33. Evolution of Mn-TM coordination number (CN) in LLO and LLOM during the first charge/discharge.
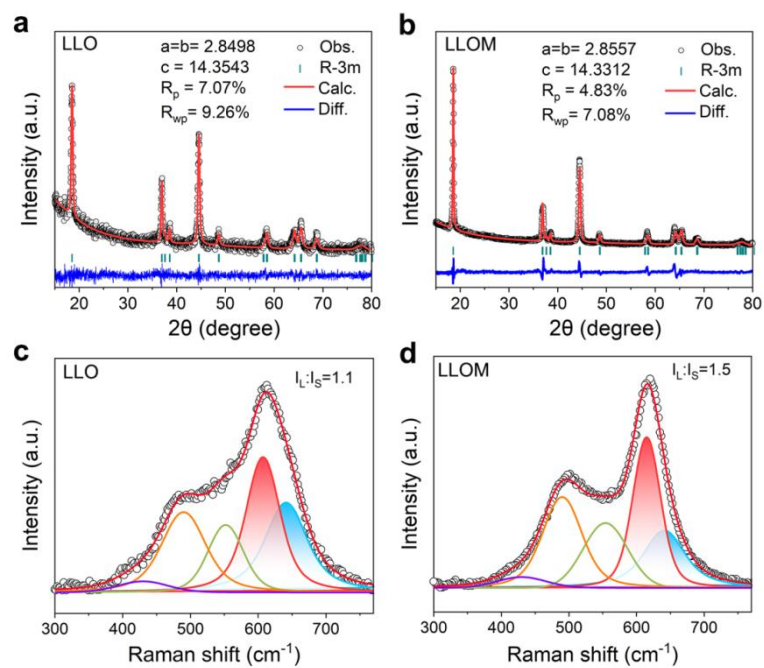
Fig. S34 Structural evolution performed of LLO and LLOM after 200 cycles. a, b) LLOR (a) and LLOM (b) Rietveld refinement XRD results through GSAS-II after 200 cycles at 1 C-rate. c, d) Raman spectra of LLO (c) and LLOM (d) and fitting results.
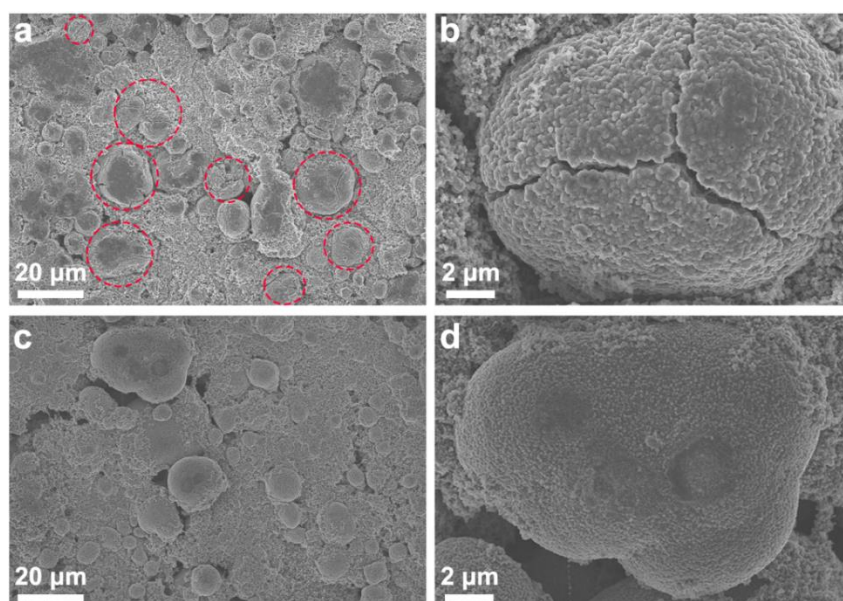
Fig. S35 Surface morphology of LLO and LOM after 200 cycles. a, b) SEM images of LLO (a) after 200 cycles at 1 C-rate and the enlarged images. c, d) SEM images of LLOM (c) after 200 cycles at 1 C-rate and the enlarged images.
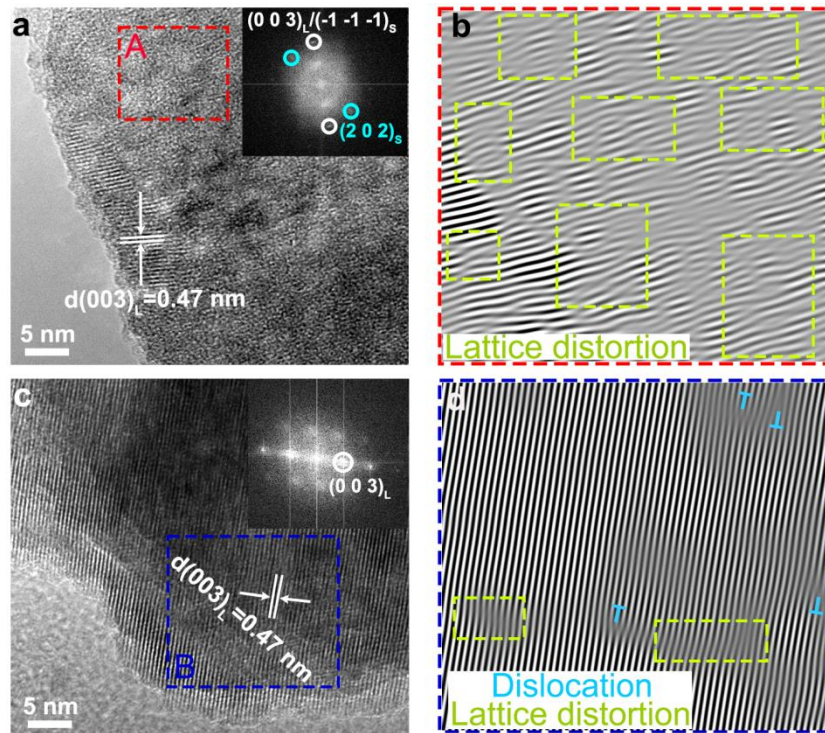
Fig. S36 Microstructure of LLO and LLOM after 200 cycles. a) TEM image of LLO electrodes after 200 cycles at 1 C-rate. b) Inverse fast Fourier transformation (IFFT) of (003) spots in the red box in (a). c) TEM image of LLOM electrodes after 200 cycles at 1 C-rate. Inverse fast Fourier transformation (IFFT) of (003) spots in the blue box in (c).

Supplementary Tables

Table S1. ICP analysis results for pristine LLO and quenched samples.

Sample	Li	Ni	Co	Mn	Mg/Al/Fe/Sr
LLO	1.187	0.136	0.136	0.533	0
LLODIW	1.180	0.136	0.136	0.536	0
LLOM	1.145	0.135	0.136	0.542	0.005 (Mg)
LLOS	1.149	0.135	0.136	0.542	0.003 (Sr)
LLOA	1.058	0.138	0.139	0.556	0.008 (Al)
LLOF	1.017	0.138	0.140	0.560	0.016 (Fe)

Table S2. ICP analysis results of the reaction filtrate for quenching of LLODIW and LLOA.

Sample	Li (μg/mL)	Ni (μg/mL)	Co (μg/mL)	Mn (μg/mL)
LLODIW- Filtrate	8.031	0.018	0.018	0.044
LLOA- Filtrate	357.899	4.100	17.998	32.801

Table S3. Refined crystallographic structural parameters of rhombohedral R-3m phase for LLO, LLODIW, LLOM, LLOS, LLOA, and LLOF samples.

	LLO	LLODIW	LLOM	LLOS	LLOA	LLOF
a (Å)	2.84982	2.85057	2.85169	2.85149	2.85193	2.85389
c (Å)	14.23830	14.23887	14.23864	14.24287	14.24501	14.25892
V (Å^3)	100.1436	100.1902	100.2584	100.2933	100.3393	100.5754
Li/Ni mixing (%)	1.03	1.15	1.84	1.59	2.71	3.01
Mustrain(%)	0.42879	0.44511	0.50389	0.46847	0.51770	0.54129

Table S4. Fitted EXAFS distortion factors (σ^2) and distances (R) for TM-O coordination shells (TM= Mn, Co, Ni). σ^2 and R represent the average interatomic distance (half-path length), and the mean square relative displacement in R (disorder).

Samples	Mn-O shell		Co-O shell		Ni-O shell	
	σ^2 (Å^2)	R (Å)	σ^2 (Å^2)	R (Å)	σ^2 (Å^2)	R (Å)
LLO	0.0005(5)	1.9042(35)	0.0004 (8)	1.9122(55)	0.0022(6)	2.0189(39)
LLODIW	0.0006(4)	1.9058(31)	0.0005(7)	1.9130(47)	0.0024(7)	2.0179(42)
LLOM	0.0008(5)	1.9067(34)	0.0008 (8)	1.9175(52)	0.0038(10)	2.0203(59)
LLOS	0.0006 (5)	1.9046(36)	0.0007 (8)	1.9113(53)	0.0031(8)	2.0191(45)
LLOA	0.0009(6)	1.9029(42)	0.0009 (9)	1.9177(58)	0.0043(9)	2.0179(50)
LLOF	0.0012(5)	1.9044(36)	0.0011(8)	1.9119(56)	0.0051(10)	2.0203(52)

Table S5. Detailed structural parameters for Joint Rietveld refinement patterns of synchrotron X-ray diffraction (SXRD) and neutron powder diffraction(NPD) for LLO material.

$Li_{1.187}Ni_{0.136}Co_{0.136}Mn_{0.533}O_2$ (LLO).　Space group: R-3m　R_{wp}= 4.42%

a=b= 2.84970(4) Å c= 14.23804(6) Å V= 101.133(11) Å^3

$S(MO_2)$=2.6373 Å　$I(LiO_2)$=2.1087 Å　$d_{(TM-O)}$=1.9541(6) Å

Atom	Wyckoff position	Coordinates			Occupancy
		X	Y	Z	
Li	3a	0.0	0.0	0.0	0.9897(11)
Ni	3a	0.0	0.0	0.0	0.0103(11)
Li	3b	0.0	0.0	0.5	0.1973(11)
Ni	3b	0.0	0.0	0.5	0.1257(11)
Co	3b	0.0	0.0	0.5	0.1360
Mn	3b	0.0	0.0	0.5	0.5330
O	6c	0.0	0.0	0.24072(7)	0.9928(6)

Table S6. Detailed structural parameters for Joint Rietveld refinement patterns of synchrotron X-ray diffraction (SXRD) and neutron powder diffraction(NPD) for LLOM materials.

$Li_{1.145}Ni_{0.135}Co_{0.136}Mn_{0.542}Mg_{0.005}O_2$ (LLOM).　Space group: R-3m　R_{wp}= 4.36%

a=b= 2.85161(8) Å　c= 14.23841(9) Å　V= 101.268(15) $Å^3$

$S(MO_2)$=2.6245 Å　$I(LiO_2)$=2.1216 Å　$d_{(TM-O)}$=1.9585(3) Å

Atom	Wyckoff position	Coordinates			Occupancy
		X	Y	Z	
Li	3a	0.0	0.0	0.0	0.9764(9)
Ni	3a	0.0	0.0	0.0	0.0184(9)
Mg	3a	0.0	0.0	0.0	0.0052(2)
Li	3b	0.0	0.0	0.5	0.1686(9)
Ni	3b	0.0	0.0	0.5	0.1166(9)
Co	3b	0.0	0.0	0.5	0.1360
Mn	3b	0.0	0.0	0.5	0.5420
O	6c	0.0	0.0	0.24117(30)	0.9520(3)

Table S7. Detailed structural parameters for Joint Rietveld refinement patterns of synchrotron X-ray diffraction (SXRD) and neutron powder diffraction(NPD) for LLOM-H materials.

LLOM-H   Space group: C2/m R_{wp}= 3.74%

a= 4.93588(5) Å   b=8.54844(6) Å c= 5.02061(4) Å

Atom	Multiplicity	Coordinates			Occupancy
		X	Y	Z	
Li0	4	0.0	0.1661	0	1
Li1	2	0.0	0.0	0.5	0.9774(4)
Li2	2	0.0	0.5	0.0	1
Mn	4	0.0	0.16706	0.5	1
O1	4	0.2190	0.0	0.2260	1
O2	8	0.2533	0.3238	0.2231	1
H	4	0.3799	0.5	0.6008	0.0226(6)

Table S8. The summary of capacity retention of rechargeable intercalation-type Li-rich cathode coin cells.

Material	Method	Initial Capacity/ICE [%]/0.1 C	Voltage/ Rate	Capacity retention (Cycle number)	Ref.
$Li_{1.145}Ni_{0.135}Co_{0.136}Mn_{0.542}O_2$	Brine quenching	302 mAh g^{-1}/88%	2-4.8 V/0.2 C	90.5% (200)	This work
$Li_{1.145}Ni_{0.135}Co_{0.136}Mn_{0.542}O_2$	Brine quenching	302 mAh g^{-1}/88%	2-4.8 V/1 C	92.3% (200)	This work
$Li_{1.145}Ni_{0.135}Co_{0.136}Mn_{0.542}O_2$	Brine quenching	302 mAh g^{-1}/88%	2-4.8 V/5 C	97.7% (200)	This work
$Li_{1.4}Mn_{0.6}Ni_{0.2}Co_{0.2}O_{2+x}$	Te^{6+}doping/Mg$_3$(PO$_2$)$_2$ coating	282.2 mAh g^{-1}/95.4%	2-4.6 V/1 C	89.2% (200)	[13]
$Li_{1.2}Mn_{0.6}Ni_{0.2}O_2$	Ti Doping/coating	269.9 mAh g^{-1}/81%	2-4.6 V/1 C	85.0% (500)	[14]
$Li_{1.2}Mn_{0.54}Ni_{0.13}Co_{0.13}O_2$	MOF-treatment/ Co-gradient	271 mAh g^{-1}/79.6%	2-4.8 V/1 C	82.7% (200)	[15]
$Li_{1.2}Mn_{0.54}Ni_{0.13}Co_{0.13}O_2$	Spinel/LiNbO$_3$ coating/Nb doping	279.8 mAh g^{-1}/84.66%	2-4.8 V/1 C	74.05% (250)	[16]
$Li_{1.2}Mn_{0.54}Ni_{0.13}Co_{0.13}O_2$	Se Doping	293.15 mAh g^{-1}/94.3%	2-4.8 V/2 C	88.4% (400)	[17]
$Li_{1.2}Mn_{0.54}Ni_{0.13}Co_{0.13}Ti_{0.01}O_2$	Surface Al doping	305 mAh g^{-1}/91%	2-4.8 V/1 C	87.4% (100)	[18]
$Li_{1.2}Mn_{0.56}Ni_{0.17}Co_{0.07}O_2$	oxygen vacancies and P doping	275 mAh g^{-1}/80.5%	2-4.8 V/1 C	78.6% (500)	[19]
$Li_{1.2}Mn_{0.533}Ni_{0.267}O_2$	La/Al cooping Li$_x$CoPO$_4$ nanocoating	253.8 mAh g^{-1}/84.68%	2-4.7 V/1 C	80.1% (500)	[20]
$Li_{1.2}Ni_{0.13}Co_{0.13}Mn_{0.53}Nb_{0.01}O_2$	Nb doping	278.1 mAh g^{-1}/84.2%	2-4.8 V/0.1 C	82.7% (100)	[21]
$Li_{1.2}Ni_{0.2}Mn_{0.6}O_2$	Li$_3$PO$_4$/Li$_x$Ni$_y$Mn$_{3-x-y}$O$_4$	302.6 mAh g^{-1}/90.3%	2-4.8 V/1 C	82.5% (300)	[22]
$Li_{1.2}Mn_{0.54}Ni_{0.13}Co_{0.13}O_2$	Spinel/S doping	289.52 mAh g^{-1}/80.19%	2-4.8 V /1 C	88.2% (200)	[23]
$Li_{1.2}Mn_{0.54}Ni_{0.13}Co_{0.13}O_2$	Li$_2$SeO$_4$/ Li$_2$Ni$_x$Co$_y$O$_4$	286 mAh g^{-1}/85.29%	2-4.8 V/1 C	80.0% (200)	[24]
$0.33Li_2MnO_3\ 0.67LiNi_{0.4}Co_{0.2}$	Na$_5$AlO$_4$ Coating	272 mAh g^{-1}/90%	2-4.8 V/1 C	61.0% (400)	[25]

$Mn_{0.4}O_2$					
$Li_{1.2}Mn_{0.54}Ni_{0.13}Co_{0.13}O_2$	Mg_2TiO_4 Coating	319 mAh g^{-1}/83%	2-4.9 V/2 C	81.0% (700)	[26]
$Li_{1.2}Mn_{0.54}Ni_{0.13}Co_{0.13}O_2$	PAA Coating	244 mAh g^{-1}/80%	2-4.8 V /100 ma/g	97.7% (100)	[27]
$Li_{1.08}Mn_{0.54}Ni_{0.13}Co_{0.13}O_2$	Li_2TiO_3 Coating	276.5 mAh g^{-1}/86.3%	2-4.8 V/1 C	87.1% (125)	[28]
$Li_{1.2}Ni_{0.16}Co_{0.16}Mn_{0.48}O_2$	Li gradient	293.1 mAh g^{-1}/90.8%	2-4.8 V/0.2 C	89.0% (200)	[29]
$Li_{1.16}Mn_{0.54}Ni_{0.21}Co_{0.08}O_2$	TM gradient	268 mAh g^{-1}/80.2%	2-4.8 V/200 ma/g	88.4% (200)	[30]
$Li_{1.2}Ni_{0.13}Co_{0.13}Mn_{0.54}O_2$	S doping	270.5 mAh g^{-1}/84.5%	2-4.6 V/0.5C	81.1% (600)	[31]
$Li_{1.13}Mn_{0.517}Ni_{0.256}Co_{0.097}O_2$	$LiTaO_3$ coating	272.8 mAh g^{-1}/83.72%	2-4.6 V/1C	85.0% (200)	[32]

Table S9. Detailed information of pouch cell.

Electrode	Cathode		Anode
	LLO	LLOM	Graphite
Active substance content [%]	92.0	92.0	93.5
Surface load mass [mg cm^{-2}]	10	10	7.8
Specific capacity [mAh g^{-1}]	250	260	350
Compaction density [g cm^{-3}]	2.3		1.6
Electrode size [mm^2]	62*72		64*74
Cell capacity [Ah]	1.32	1.6	
N/P ratio	1.07	1.07	
Energy density [Wh kg^{-1}]	210.3	210.6	

Table S10. The summary of capacity retention of rechargeable intercalation-type Li-rich cathode pouch cells.

Material	Method	Cell capacity (mAh)	Voltage/Rate	Capacity retention (Cycle number)	Ref.
$0.35Li_2MnO_3 \cdot 0.65LiNi_{0.35}Mn_{0.45}Co_{0.20}O_2$	$Li_xSi_yO_z$ Coating	6	2-4.6 V/0.33 C	81.4%(200)	[33]
$Li_{1.167}Mn_{0.575}Ni_{0.25}O_2$	K^+ doping	6	2-4.6 V/0.1 C	74.9%(100)	[34]
$Li_{1.11}Mn_{0.49}Ni_{0.29}Co_{0.11}O_2$	Structural design	12	2-4.55 V/100 mA/g	83.1%(100)	[35]
$Li_{1.14}Ni_{0.13}Co_{0.13}Mn_{0.54}O_2$	$NaVO_3$ Coating	15.1	2-4.5 V/1 C	80.4%(400)	[36]
$Li_{1.2}Mn_{0.6}Ni_{0.2}O_2$	LiPP Coating	40	2-4.7 V/40 mA/g	74.5%(100)	[37]
$Li_{1.2}Mn_{0.6}Ni_{0.2}O_2$	molten-molybdate treatment	99	2.8-4.65 V/1 C	76.0%(125)	[38]
$Li_{1.144}Ni_{0.136}Co_{0.136}Mn_{0.544}O_2$	Electrolyte Modification	270	2-4.55 V/0.5 C	91.1%(50)	[39]
$Li_{1.2}Ni_{0.25}Mn_{0.55}O_2$	LiOH additive	400	2-4.5 V/0.5 C	87.6%(500)	[40]
$Li_{1.2}Ni_{0.25}Mn_{0.55}O_2$	Adjusting cutoff voltage	400	2-4.5 V/0.5 C	84.2%(900)	[40]
$Li_{1.2}Mn_{0.56}Ni_{0.16}Co_{0.08}O_2$	Na^+ doping	650	2.5-4.6 V/2 C	77.0%(500)	[41]
$Li_{1.3}Mn_{0.7}Ni_{0.2}Co_{0.1}O_{2.4}$	Ni/Mn component modulation	770	2.5-4.6 V/1 C	90.0%(300)	[42]
$Li_{1.2}Mn_{0.56}Ni_{0.16}Co_{0.08}O_2$	W^{6+} doping	840	2.5-4.55 V/1 C	87.7%(500)	[43]
$Li_{1.2}Mn_{0.56}Ni_{0.16}Co_{0.08}O_2$	Pre-oxidation of precursor	1000	2-4.55V/2C	81.6%(500)	[44]
$Li_{1.08}Ni_{0.22}Co_{0.22}Mn_{0.45}O_2$	ALD Coating of Al_2O_3	1250	2-4.55 V/0.5 C	80.4%(710)	[45]

$Li_{1.144}Ni_{0.136}Co_{0.136}Mn_{0.544}O_2$	Electrolyte Modification	1800	2-4.6 V/0.2 C	80.0%(600)	[46]
$Li_{1.14}Ni_{0.13}Co_{0.13}Mn_{0.54}O_2$	Non-eutectic-salt treatment	2100	2-4.55 V/0.33 C	78.6%(300)	[47]
$Li_{1.2}Ni_{0.267}Mn_{0.533}O_2$	Electrolyte Modification	2500	2.5-4.55 V/1 C	91.1%(200)	[48]
$Li_{1.14}Ni_{0.22}Co_{0.12}Mn_{0.52}O_2$	N/A	6910	2-4.6 V/0.2 C	80.0%(350)	[49]
$Li_{1.14}Ni_{0.13}Co_{0.13}Mn_{0.54}O_2$	Electrolyte design	157.21	2-4.6V/0.5C	80.0%(150)	[50]
$Li_{1.145}Ni_{0.135}Co_{0.136}Mn_{0.542}O_2$	Brine quenching	1600	2-4.6V/0.33 C	80.0%(2065)	This work
$Li_{1.145}Ni_{0.135}Co_{0.136}Mn_{0.542}O_2$	Brine quenching	1600	2-4.55 V/1 C	80.0%(2159)	This work
$Li_{1.145}Ni_{0.135}Co_{0.136}Mn_{0.542}O_2$	Brine quenching	1600	2-4.55 V/1 C	72.1%(3200)	This work

Table S11. EXAFS fits of the Mn *K*-edge from the LLO and LLOM electrode during the first charge-discharge cycle. R-factor indicates the goodness-of-fit. For each individual path, R and σ^2 represent the average interatomic distance (half-path length), and the mean square relative displacement in R (disorder). The coordination numbers (CNs) for were fixed.

Mn-O CN=6							
LLO				LLOM			
E(V)	R (Å)	σ^2 (Å^2)	R-factor	E(V)	R (Å)	σ^2 (Å^2)	R-factor
OCV	1.9046(101)	0.0006(7)	0.008	OCV	1.9050(111)	0.0009(8)	0.009
cha. 4.4 V	1.8944(90)	0.0023(6)	0.005	cha. 4.4 V	1.8971(100)	0.0019(7)	0.007
cha. 4.8 V	1.8981(40)	0.0039(6)	0.006	cha. 4.8 V	1.8957(95)	0.0032(6)	0.005
dis. 3.2 V	1.8962(37)	0.0030(6)	0.006	dis. 3.2 V	1.8986(108)	0.0027(7)	0.006
dis. 2.0 V	1.9052 (89)	0.0016(6)	0.005	dis. 2.0 V	1.9040(43)	0.0012(6)	0.009

Table S12. EXAFS fits of the Co *K*-edge from the LLO and LLOM electrode during the first charge-discharge cycle. R-factor indicates the goodness-of-fit. For each individual path, R and σ^2 represent the average interatomic distance (half-path length), and the mean square relative displacement in R (disorder). The coordination numbers (CNs) for were fixed.

Co-O	CN=6						
	LLO				LLOM		
E(V)	R (Å)	σ^2 (Å^2)	R-factor	E(V)	R (Å)	σ^2 (Å^2)	R-factor
OCV	1.9118(154)	0.0004(11)	0.008	OCV	1.9098(65)	0.0005(10)	0.012
cha. 4.4 V	1.8924(148)	0.0009(10)	0.007	cha. 4.4 V	1.8816(178)	0.0010(11)	0.011
cha. 4.8 V	1.9032(97)	0.0005(7)	0.009	cha. 4.8 V	1.8998(101)	0.0004(7)	0.009
dis. 3.2 V	1.9003(166)	0.0016(11)	0.008	dis. 3.2 V	1.9146(158)	0.0013(11)	0.009
dis. 2.0 V	1.9103(155)	0.0009(10)	0.009	dis. 2.0 V	1.9098(147)	0.0004(10)	0.008

Table S13. EXAFS fits of the Ni *K*-edge from the LLO and LLOM electrode during the first charge-discharge cycle. R-factor indicates the goodness-of-fit. For each individual path, R and σ^2 represent the average interatomic distance (half-path length), and the mean square relative displacement in R (disorder). The coordination numbers (CNs) for were fixed.

				Ni-O CN=6			
	LLO				LLOM		
E(V)	R (Å)	σ^2 (Å^2)	R-factor	E(V)	R (Å)	σ^2 (Å^2)	R-factor
OCV	2.0351(209)	0.00275(16)	0.009	OCV	2.0278(224)	0.00297(17)	0.010
cha. 4.4 V	1.8997(151)	0.00587(10)	0.004	cha. 4.4 V	1.8945(146)	0.00525(10)	0.006
cha. 4.8 V	1.9177(149)	0.00347(24)	0.020	cha. 4.8 V	1.9160(101)	0.00310(16)	0.019
dis. 3.2 V	1.9574(111)	0.00785(19)	0.016	dis. 3.2 V	1.9926(111)	0.00711(20)	0.010
dis. 2.0 V	2.0054(99)	0.00537(16)	0.027	dis. 2.0 V	2.0059(89)	0.00244(16)	0.009

Table S14. Fitted EXAFS coordination numbers (CN) for Mn-TM coordination in LLO and LLOM during the first charge/discharge.

E(V)	LLO (CN)	LLOM (CN)
OCV	3.525(25)	3.486(25)
cha. 4.4 V	3.777(27)	3.867(27)
cha. 4.8 V	6.034(42)	6.117(43)
dis. 3.2 V	5.396(37)	5.079(36)
dis. 2.0 V	3.970(28)	3.544(28)

Table S15. Results of the Rietveld analysis for LLO and LLOM after 200 cycles at 1C from GSAS-II.

Sample	a (Å)	a (Å)	$I_{(003)}/I_{(104)}$	R_{wp}/%	R_p/%
LLO	2.8498	14.3543	1.3745	9.26	7.07
LLOM	2.8557	14.3312	1.9636	7.08	4.83

References

1. B. Qiu, M. Zhang, L. Wu, J. Wang, Y. Xia, D. Qian, H. Liu, S. Hy, Y. Chen, K. An, Y. Zhu, Z. Liu and Y. S. Meng, *Nat. Commun.*, 2016, **7**, 12108.

2. B. Ravel and M. Newville, *Journal of Synchrotron Radiation*, 2005, **12**, 537-541.

3. B. Gilbert, B. H. Frazer, A. Belz, P. G. Conrad, K. H. Nealson, D. Haskel, J. C. Lang, G. Srajer and G. De Stasio, *J. Phys. Chem. A*, 2003, **107**, 2839-2847.

4. B. H. Toby and R. B. Von Dreele, *J. Appl. Crystallogr.*, 2013, **46**, 544-549.

5. G. Kresse and D. Joubert, *PhRvB*, 1999, **59**, 1758-1775.

6. G. Kresse and J. Hafner, *PhRvB*, 1993, **47**, 558-561.

7. J. P. Perdew, K. Burke and M. Ernzerhof, *Phys. Rev. Lett.*, 1996, **77**, 3865-3868.

8. F. Zhou, M. Cococcioni, C. A. Marianetti, D. Morgan and G. Ceder, *PhRvB*, 2004, **70**, 235121.

9. H. J. Monkhorst and J. D. Pack, *PhRvB*, 1976, **13**, 5188-5192.

10. H. Zheng, Z. Hu, P. Liu, W. Xu, Q. Xie, W. He, Q. Luo, L. Wang, D. Gu, B. Qu, Z.-Z. Zhu and D.-L. Peng, *Energy Stor. Mater.*, 2020, **25**, 76-85.

11. B. Qiu, Q. Zhang, H. Hu, J. Wang, J. Liu, Y. Xia, Y. Zeng, X. Wang and Z. Liu, *Electrochim. Acta*, 2014, **123**, 317-324.

12. W. B. Jensen, *J. Chem. Educ.*, 1995, **72**, 395.

13. R. Yu, M. N. Banis, C. Wang, B. Wu, Y. Huang, S. Cao, J. Li, S. Jamil, X. Lin, F. Zhao, W. Lin, B. Chang, X. Yang, H. Huang, X. Wang and X. Sun, *Energy Stor. Mater.*, 2021, **37**, 509-520.

14. D. Luo, J. Cui, B. Zhang, J. Fan, P. Liu, X. Ding, H. Xie, Z. Zhang, J. Guo, F. Pan and Z. Lin, *Adv. Funct. Mater.*, 2021, **31**, 2009310.

15. H. Wang, F. Liu, R. Yu, Z. Xiao, Z. Zhu, L. Zhou and J. Wu, *Nano Energy*, 2022, **100**, 107439.

16. C. Shen, Y. Liu, L. Hu, W. Li, X. Liu, Y. Shi, Y. Jiang, B. Zhao and J. Zhang, *Nano Energy*, 2022, **101**, 107555.

17. J. Chen, H. Chen, W. Deng, X. Gao, S. Yin, Y. Mei, S. Zhang, L. Ni, J. Gao, H.

Liu, Y. Tian, L. Yang, X. Deng, G. Zou, H. Hou, J. Xie and X. Ji, *Energy Stor. Mater.*, 2022, **51**, 671-682.

18. S. Li, L. Yang, Z. Liu, C. Zhang, X. Shen, Y. Gao, Q. Kong, Z. Hu, C.-Y. Kuo, H.-J. Lin, C.-T. Chen, Y. Yang, J. Ma, Z. Hu, X. Wang, R. Yu, Z. Wang and L. Chen, *Energy Stor. Mater.*, 2023, **55**, 356-363.

19. Z. Wang, Y. Yin, G. He, H. Zhao and Y. Bai, *Nanoscale*, 2023, **15**, 588-598.

20. G. Zhou, D. Zhang, Y. Zhang, W. Wang, T. Uchiyama, C. Zhang, Y. Uchimoto and W. Wei, *ACS Appl. Mater. Interfaces*, 2023, **15**, 19055-19065.

21. S. Yun, J. Yu, W. Lee, H. Lee and W.-S. Yoon, *Materials Horizons*, 2023, **10**, 829-841.

22. W. Zeng, F. Liu, J. Yang, B. Zhang, F. Cao, W. Tian, J. Wang, R. Yu, F. Xia, H. Peng, J. Ma, Z. Wang, S. Mu and J. Wu, *Energy Stor. Mater.*, 2023, **54**, 651-660.

23. X. Ji, Y. Xu, Q. Xia, Y. Zhou, J. Song, H. Feng, P. Wang, J. Yang and Q. Tan, *ACS Appl. Mater. Interfaces*, 2022, **14**, 30133-30143.

24. T. Wang, W. Zeng, J. Zhu, W. Tian, J. Wang, J. Tian, D. Yuan, S. Zhang and S. Mu, *Nano Energy*, 2023, **113**, 108577.

25. S. Maiti, H. Sclar, R. Sharma, N. Vishkin, M. Fayena-Greenstein, J. Grinblat, M. Talianker, L. Burstein, N. Solomatin, O. Tiurin, Y. Ein-Eli, M. Noked, B. Markovsky and D. Aurbach, *Adv. Funct. Mater.*, 2021, **31**, 2008083.

26. W. Zhang, Y. Sun, H. Deng, J. Ma, Y. Zeng, Z. Zhu, Z. Lv, H. Xia, X. Ge, S. Cao, Y. Xiao, S. Xi, Y. Du, A. Cao and X. Chen, *Adv. Mater.*, 2020, **32**, 2000496.

27. J. Yang, P. Li, F. Zhong, X. Feng, W. Chen, X. Ai, H. Yang, D. Xia and Y. Cao, *Adv. Energy. Mater.*, 2020, **10**, 1904264.

28. J. Liu, Z. Wu, M. Yu, H. Hu, Y. Zhang, K. Zhang, Z. Du, F. Cheng and J. Chen, *Small*, 2022, **18**, 2106337.

29. Z. Zhu, D. Yu, Y. Yang, C. Su, Y. Huang, Y. Dong, I. Waluyo, B. Wang, A. Hunt, X. Yao, J. Lee, W. Xue and J. Li, *Nat. Energy*, 2019, **4**, 1049-1058.

30. T. Wu, X. Liu, X. Zhang, Y. Lu, B. Wang, Q. Deng, Y. Yang, E. Wang, Z. Lyu,

Y. Li, Y. Wang, Y. Lyu, C. He, Y. Ren, G. Xu, X. Sun, K. Amine and H. Yu, *Adv. Mater.*, 2021, **33**, 2001358.

31.   Z. Sun, L. Xu, C. Dong, H. Zhang, M. Zhang, Y. Ma, Y. Liu, Z. Li, Y. Zhou, Y. Han and Y. Chen, *Nano Energy*, 2019, **63**, 103887.

32.   E. Wang, Y. Zhao, D. Xiao, X. Zhang, T. Wu, B. Wang, M. Zubair, Y. Li, X. Sun and H. Yu, *Adv. Mater.*, 2020, **32**, 1906070.

33.   Rosy, S. Haber, E. Evenstein, A. Saha, O. Brontvein, Y. Kratish, D. Bravo-Zhivotovskii, Y. Apeloig, M. Leskes and M. Noked, *Energy Stor. Mater.*, 2020, **33**, 268-275.

34.   C. Liu, M. Wu, S. Hang, T. Xu, G. Yang, H. Ji and Y. Yang, *J. Alloys Compd.*, 2019, **787**, 700-710.

35.   J. Hwang, S. Myeong, E. Lee, H. Jang, M. Yoon, H. Cha, J. Sung, M. G. Kim, D.-H. Seo and J. Cho, *Adv. Mater.*, 2021, **33**, 2100352.

36.   Y. Qu, W. Tang, H. Liu, C. Li, L. Zou, Z. Chen, Z. Yang, J. Su and W. Zhang, *Ind. Eng. Chem. Res.*, 2023, **62**, 10467-10476.

37.   R. Zhao, M. Wu, P. Jiao, X. Wang, J. Zhu, Y. Zhao, H. Zhang, K. Zhang, C. Li, Y. Ma and Y. Chen, *Nano Res.*, 2023, **16**, 6805-6814.

38.   Z. Zhu, R. Gao, I. Waluyo, Y. Dong, A. Hunt, J. Lee and J. Li, *Adv. Energy. Mater.*, 2020, **10**, 2001120.

39.   Y. Li, W. Li, R. Shimizu, D. Cheng, H. Nguyen, J. Paulsen, S. Kumakura, M. Zhang and Y. S. Meng, *Adv. Energy. Mater.*, 2022, **12**, 2103033.

40.   J. Xiong, Z. Liang, Q. Guo, M. Zhou, H. Potapenko and S. Zhong, *Energy Fuels*, 2021, **35**, 15143-15152.

41.   Q. Ma, Z. Chen, S. Zhong, J. Meng, F. Lai, Z. Li, C. Cheng, L. Zhang and T. Liu, *Nano Energy*, 2021, **81**, 105622.

42.   Z. Chen, J. Meng, Y. Wang, Q. Ma, F. Lai, Z. Li, Q. Zhang, D. Li and S. Zhong, *Electrochim. Acta*, 2021, **378**, 138138.

43.   J. Meng, L. Xu, Q. Ma, M. Yang, Y. Fang, G. Wan, R. Li, J. Yuan, X. Zhang, H. Yu, L. Liu and T. Liu, *Adv. Funct. Mater.*, 2022, **32**, 2113013.

44.   J. Meng, H. Xu, Q. Ma, Z. Li, L. Xu, Z. Chen, B. Cheng and S. Zhong,

Electrochim. Acta, 2019, **309**, 326-338.

45.   Y. Li, Z. Shi, B. Qiu, J. Zhao, X. Li, Y. Zhang, T. Li, Q. Gu, J. Gao and Z. Liu, *Adv. Funct. Mater.*, 2023, **33**, 2302236.

46.   X. Yao, H. Ma, L. Guo, L. Huang and W. Qian, *Ionics*, 2023, **29**, 4577-4584.

47.   T. Li, Z. Shi, L. Li, Y. Zhang, Y. Li, J. Zhao, Q. Gu, W. Wen, B. Qiu and Z. Liu, *Chem. Eng. J.*, 2023, **474**, 145728.

48.   Z. Lu, D. Liu, K. Dai, K. Liu, C. Jing, W. He, W. Wang, C. Zhang and W. Wei, *Energy Stor. Mater.*, 2023, **57**, 316-325.

49.   L. Kraft, T. Zünd, D. Schreiner, R. Wilhelm, F. J. Günter, G. Reinhart, H. A. Gasteiger and A. Jossen, *J. Electrochem. Soc.*, 2021, **168**, 020537.

50.   Y. Wang, Z. Li, X. Li, Z.-F. Ma and L. Li, *Adv. Energy. Mater.*, **n/a**, 2304512.